Measurement-based Assessment of Space Diversity for Indoor Fixed Wireless Channels

by

Chengyu Wang

A THESIS SUBMITTED IN PARTIAL FULFILMENT OF
THE REQUIREMENTS FOR THE DEGREE OF

MASTER OF APPLIED SCIENCE

in

THE FACULTY OF GRADUATE STUDIES

ELECTRICAL AND COMPUTER ENGINEERING

THE UNIVERSITY OF BRITISH COLUMBIA

April 22, 2005

Abstract

We have employed a measurement-based approach to investigate the effectiveness of space diversity in indoor fixed wireless environments where body shadowing (blockage of the line-of-sight between the transmitter and receiver by the movement of people) is a significant impairment. In order to assist those planning measurement campaigns in indoor fixed wireless environments, we present simulation results that give the sample duration required to accurately estimate path gain and Rician K-factor given the parameters of the Doppler spectrum (type and cut-off) and the sample rate. Next, we present measurement results that show the received signal envelope generally follows the Rician distribution when people move between the transmitter and receiver. We also reveal details of the manner in which body shadowing affects the shape of the Doppler spectrum observed in indoor fixed environments. In particular, we show that body movement can give rise to small sidebands in the Doppler spectrum. Finally, we compare theoretical predictions of spatial correlation as a function of antenna spacing to the measurement results and found reasonable agreement. The results give us confidence that our measurement system is suitable for use in more ambitious measurement campaigns in the future. Finally, we show how measurement-based models could be used in dynamic simulations of space diversity channels in indoor fixed wireless environments.

Contents

List of Tables

List of Figures

Acknowledgements

First of all, I would like to express my sincere thanks to my supervisor, Professor Dave Michelson, for his constant encouragement, insightful comments, and invaluable guidance, which benefited not only the work presented in this thesis, but also my future career.

I would like to thank Professor Cyril Leung and Professor Robert Schober for serving on my thesis committee, reading my thesis and offering great comments.

I would also like to express my appreciation to my fellow graduate students in the Radio Science Lab, especially Steven Ma, Jessie Liu, Chris Hynes, Nima Mahanfar and James Chuang for their thought provoking discussions and technical assistance with this research. Also my gratitude goes to Howard Huang, Anthony Liou, William Shih and my other lab mates for helping me set up the measurement platform and collect data.

Finally, I would like to thank my parents for their love and continuous support. Many thanks to my wife, Jin Yang, for her love, encouragement, support and understanding as I pursued graduate studies.

Chapter 1

Introduction

1.1 Statement of Problem

This thesis is concerned with measurement-based characterization of the manner in which body shadowing (blockage of the line-of-sight between the transmitter and receiver by the movement of people) affects the indoor fixed wireless channel, including estimation of fading statistics, time variation (*i.e.*, Doppler spread), and space diversity correlation.

1.2 Background

In recent years, there has been significant growth in the use of short range wireless technologies, *e.g.*, Bluetooth personal area networks (PANs) and IEEE 802.11 wireless local area networks (WLANs). Bluetooth is primarily designed for replacing cables between electronic devices such as mobile phone, computers, printers, and other equipment. WLANs provide high-speed data transfer within a small area, for instance, an office building or university campus.

Short range wireless communications systems are often employed in indoor environments. Such environments are typically characterized by a large number of reflectors and scatterers. As a consequence, a signal transmitted over indoor radio channel interacts with the environment in a very complicated way. For example, the transmitted radio signal will be reflected by the walls and floors, diffracted by furniture and scattered by moving people.

The indoor radio channel differs from the traditional mobile radio channel in two aspects: (1) the distances covered are much smaller, *e.g.*, of the order of 10 metres and (2) the variability of the environment is much greater, *e.g.*, ranging from Rayleigh to Rician. In most cases, signals travel from the transmitter to the receiver via multiple paths. When the amplitude and phase of the different signal paths change, multipath fading occurs. In general, there are two primary indoor radio propagation scenarios. In the first, the transmitter (or the receiver) is located at a fixed position, while the other is moving. This type of scenario has been extensively investigated in the context of cellular wireless applications. In the second, the transmitter and receiver are both stationary but reflectors such as people move. We describe this type of radio channel as an indoor fixed wireless channel.

It is well known that multipath fading can cause significant impairment to the quality of communications over radio channels. Diversity reception is a powerful technique for overcoming these impairments at a relatively low cost. It exploits the randomness in signal propagation over different wireless channels to establish independent (or at least highly uncorrelated) signal paths, so the probability of a deep fade occurring in all of the channels simultaneously is largely reduced. There are a number of popular forms of diversity reception, such as space, polarization, frequency and time diversity [1]. Among these four diversity forms, space diversity is the most popular for indoor applications because it is easily implemented and relatively inexpensive. Here, the antennas are separated in space sufficiently so that the diversity system can achieve independent (or, at least, highly uncorrelated) fading signals over different antenna branches. The signals provided by each of the antenna branches can be combined using different diversity combining techniques such as selection diversity, maximal-ratio combining and equal gain combining, which are described in detail in [1]. Selection diversity is the least complicated of the three types of combining techniques. The algorithm for selection diversity is based upon the principle of

selecting the strongest signal from all the diversity branches at the receiver. In this thesis work, only selection diversity is considered.

1.3 Overview of Related Work

1.3.1 Factors that Affect Space Diversity Performance

The performance of space diversity can be quantified in terms of diversity gain, which permits a direct comparison of the improvement offered by multiple antennas compared to just one. The diversity gain for a given outage probability P_0 is given by [2]

$$G(P_0) = 20 \log_{10} \left[\frac{F^{-1}(P_0)}{F_1^{-1}(P_0)} \right] \tag{1.1}$$

where $F_1(x)$ is the cumulative probability distribution function (CDF) of the received signal envelope of a single branch and $F(x)$ is the CDF of the combined signal envelope. $F^{-1}(\cdot)$ is the inverse function operator. Here, the outage probability is defined as the probability of either signal-to-noise ratio (SNR) or received signal power that is less than their respective predetermined threshold values. From the Eqn. 1.1, we can see that diversity gain $G(P_0)$ is an indication of how many dB of improvement can be achieved by employing the diversity technique for a given outage probability P_0.

It is well known that diversity gain is a function of the spatial correlation between the branch envelopes and that it decreases with increasing correlation. In space diversity, the correlation between the branch envelopes can be treated as a function of the antenna spacing and angle spread of incoming waves; the general trend is that correlation decreases as the values of those two parameters increases [3]. Other factors, *e.g.*, mutual coupling and azimuthal angle of arrival (AoA), can also affect the spatial correlation.

Antenna Spacing : Clarke [4] developed a theoretical relationship between spatial

correlation and antenna spacing by assuming 2-D isotropic scattering model, *i.e.*, a uniform AoA distribution over $[-\pi, \pi]$. The resulting relationship is given in terms of a zero-order Bessel function of the first kind, as plotted in Figure 1.1,

$$\rho(d) = J_0^2(2\pi\frac{d}{\lambda}) \tag{1.2}$$

where d is antenna spacing and λ is the wavelength.
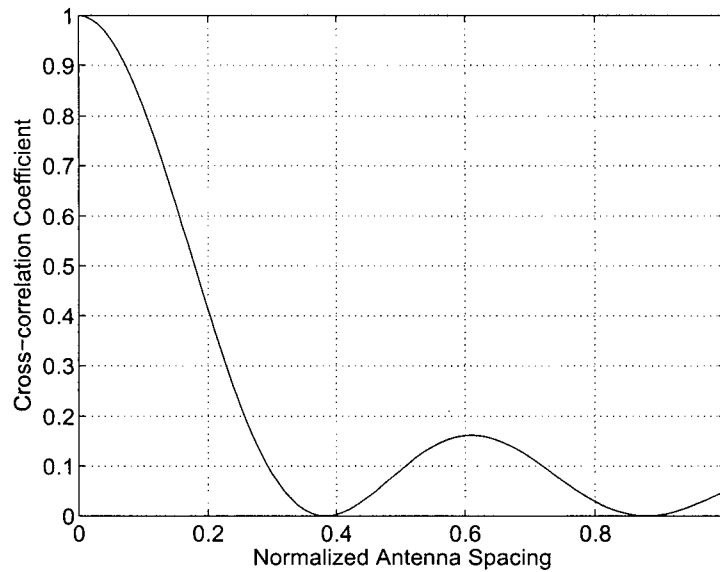
Figure 1.1: Spatial correlation vs. antenna spacing for a uniform angle of arrival distribution

The first null in the spatial correlation appears at $d = 0.38\lambda$, and after the first null, the correlation coefficient begins a damped oscillation with increasing antenna separation. This relationship is the theoretical foundation of the most popular implementation of space diversity in current wireless communication systems.

Angle Spread : In a radio environment, fading may be caused by destructive interference between multiple replicas of the transmitted signal arriving at the receiver from different angles. The azimuthal AoA is a random variable whose distribution

depends on the scattered environment. Angle spread is defined to be the variance of such distribution as a measure of the energy of distribution [3]. It is well-known that the angle spread directly affects the spatial correlation of the received signal envelopes: the larger angle spread results in lower correlation and vice-versa.

Mutual Coupling : Because mutual coupling affects the free space patterns of antennas that are sufficiently close to each other, it can significantly affect spatial correlation as well. The theoretical result shown in Eqn. 1.2, is based on an assumption of omnidirectional antenna patterns. However, in practice, when two antennas are installed with a separation of less than half of a wavelength, the antenna patterns will be distorted by the effect of mutual coupling. Consequently, the spatial correlation between the two antennas tend to decrease [5]. This is because that with small antenna spacing mutual coupling effect will tend to deform antenna patterns, *e.g.*, omnidirectional pattern of dipole antenna in this thesis work, to generate a pattern diversity-like scheme. The pattern influenced by mutual coupling has a different response for different AoAs of incoming waves. As a result, the antenna pattern distortion reduces the correlation between the branch envelopes.

Angel of Arrival : Besides the factors mentioned above, the centroid of the incoming signal AoA distribution is also considered to be a critical factor which can affect the spatial correlation. In [6], the effect of AoA on the correlation between space diversity antennas at cellular base stations was presented. Overall, the correlation will increase when the incoming signal AoA changes from broadside incidence to incidence along the array axis.

1.3.2 Previous Work Concerning Indoor Space Diversity

The effectiveness of space diversity in outdoor mobile environments and the relationship between antenna spacing, branch envelope correlation and diversity gain. has been extensively investigated. However, comparatively less information concerning

indoor environments over the UHF band (300 MHz to 3 GHz) can be found in the literature.

Lemieux *et al.* [7] conducted a series of experiments to evaluate the relative merits of space, frequency and polarization diversity in the indoor mobile environment at 900 MHz. Based on these measurements, they concluded that received signals by two antennas become decorrelated when the antenna spacing is over 0.75 wavelength. In [8], the authors experimentally investigated the space diversity performance under indoor fading conditions due to the motion of a portable terminal and the movement of people. Their results showed that the average space diversity gain achievable at 99% availability is around 10 dB for antenna spacing over 0.25 wavelength.

However both experimental studies mentioned above were conducted to investigate the space diversity performance over indoor mobile wireless channels, in which the transmitter (or the receiver) is fixed but the other is moving. Thus their experimental results can not be directly applied to our study concerning the indoor fixed wireless environments, in which both transmitter and receiver are stationary.

In [9], a three-dimensional ray-tracing modeling technique was employed to characterize indoor space diversity. According to their results, good diversity gains can be obtained with small antenna spacings, *e.g.*, 0.4 λ, and 0.75 - 1 λ antenna spacings are nearly sufficient to achieve optimum diversity performance. One hybrid model, which consisted of a two-dimensional site-specific model and a scattering model, was proposed in [2] to study space diversity in indoor environments by the ray-tracing method. Their results indicated that good diversity gains can be obtained with antenna spacings equal to or greater than one wavelength.

The accuracy of the ray-tracing method depends upon the size of local scatterers as compared to the wavelength of operation [10]. In indoor environments, the geometrical dimensions of most objects are often of the order of the wavelength of signals in the popular licence-exempt band at 2.4 GHz. Consequently, the estimation accuracy

of spatial correlation by ray-tracing modeling [2, 9] will be limited for indoor fixed wireless channels. In addition, since the local scatterers in indoor environments are much more complicated than outdoor scenarios, it will be more difficult to model the actual indoor environment precisely. This fact also degrades the estimation accuracy of ray-tracing modeling.

1.4 Objective and Approach

The objective of this thesis is to determine the manner in which body shadowing affects the indoor fixed wireless channel, including estimation of fading statistics, time variation (*i.e.*, Doppler spread), and space diversity correlation. To accomplish this, we employ a combination of computer simulation and experimental measurement techniques.

1.5 Organization of the Thesis

The remainder of this thesis is organized as follows:

- In Chapter 2, we present simulation results that give the sample duration required to accurately estimate path gain and Rician K-factor given the parameters of the Doppler spectrum (type and cut-off) and the sample rate. This is a useful result for those planning measurement campaigns in indoor fixed wireless environments.

- In Chapter 3, we describe a measurement campaign used to investigate the nature of the narrowband fixed indoor wireless channel. We present measurement results that reveal the first-order statistics of the signal envelope when people move between the transmitter and receiver. We also reveal details of the manner in which body shadowing affects the shape of the Doppler spectrum observed

in indoor fixed environments. Finally, we compare theoretical predictions of spatial correlation as a function of antenna spacing to the measurement results and found reasonable agreement.

- In Chapter 4, we show how measurement-based models could be used in dynamic simulations of space diversity channels in indoor fixed wireless environments. To find out how many dB improvement is achievable by using space diversity, we develop and validate a computer simulation approach which is based on the measured results as simulation inputs.

- Finally, Chapter 5 presents the conclusions of this thesis and offers some suggestions for future work.

Chapter 2

Estimation of the Rician K-factor from a Finite Number of Samples

2.1 Introduction

It is commonly assumed that the envelope of a fading signal follows either a Rayleigh or Rician distribution [11]. In an environment that consists of many approximately equal amplitude and uniformly distributed phase replicas of the transmitted signal arriving at the receiver, the fading envelope will have a Rayleigh probability density function (PDF),

$$p(r) = \frac{2r}{\Omega} \exp\left(-\frac{r^2}{\Omega}\right) \qquad (r \geq 0) \tag{2.1}$$

where $\Omega = E[r^2]$ is the average envelope power. When a line-of-sight (LOS) or at least a dominant specular component exists, the fading envelope will have a Rician PDF [12],

$$p(r) = \frac{2(K + 1)r}{\Omega} \exp\left(-K - \frac{(K + 1)r^2}{\Omega}\right) I_0\left(2r\sqrt{\frac{K(K + 1)}{\Omega}}\right) \qquad (r \geq 0) \tag{2.2}$$

where $I_0(.)$ is the zero-order modified Bessel function of the first kind, K is Rician K-factor defined as the ratio of the power in the specular or fixed component to the power in the multipath components and Ω is the average envelope power. Figure 2.1 shows the Rician PDF for several values of K. For $K = 0$, $i.e.$, there is no specular or fixed component and the Rician distributed envelope reduces to the Rayleigh distribution.

In an indoor fixed wireless environment, there will sometimes be a LOS signal
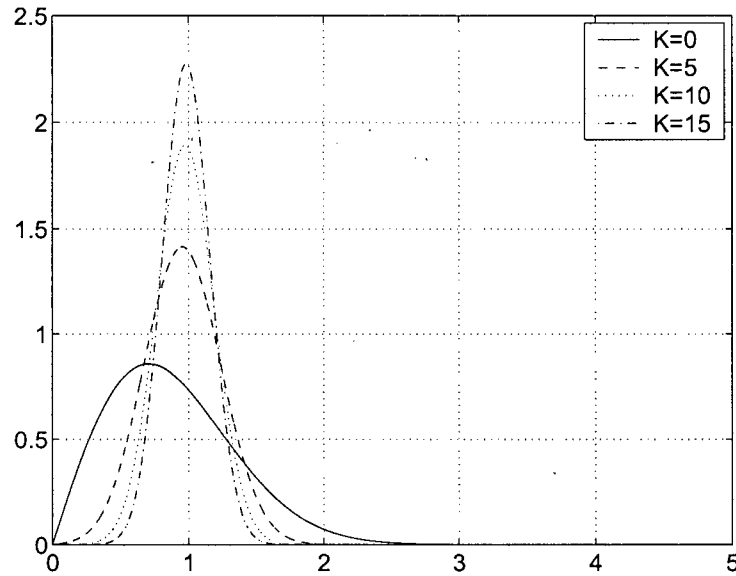
Figure 2.1: The Rician PDF for several values of K with $\Omega = 1$

path between the transmitter and receiver, at other times there will be no LOS signal path, *i.e.*, non-LOS (NLOS) propagation environment. However, even under NLOS conditions, there often exists a dominant reflected or diffracted path between the transmitter and receiver. The LOS or dominant reflected or diffracted path produces the fixed component and the summation of other weaker signal components contribute to the multipath component of the received envelope. Thus, in such an environment, the received signal envelope often experiences Rician distributed fading. This argument will be confirmed by the measurement results presented in Section 3.4.

As an important measure of fading, Rician K-factor is often used to characterize the radio environment. In this thesis work, we employ this measure to estimate the fading characteristics of the received signal envelope over indoor fixed wireless channels. Thus it is critical to achieve an accurate estimation of the Rician K-factor based upon a finite number of measured and possibly correlated samples. If the received signal envelope actually follows a Rayleigh distribution, the resulting K-factor will be zero.

In the literature, Rician K-factor estimation methods have been classified into two categories. The first are in-phase and quadrature-phase (I/Q) component-based estimators and the second are envelope-based estimators. Tepedelenlioglu *et al.* [13] proposed an approach for estimating K-factor from the I/Q components of the received signal. They show that the I/Q components-based estimator yields more accurate estimation than an envelope-based estimator, especially for small values of K. However, because we cannot extract phase information from our measured power envelope, we cannot use the I/Q component-based estimation approach here.

There have been several envelope-based estimators proposed in the literature. Among them, two estimators [14, 15] outperform others in terms of simplicity and accuracy [16]. In [14], a moment-based estimator that utilizes the first- and second-order moments ($E[r]$ and $E[r^2]$) of the received envelope is proposed. Greenstein, Michelson and Erceg [15] propose a simpler moment-based approach which uses the second- and fourth-order moments ($E[r^2]$ and $E[r^4]$) of the envelope. Compared to the first estimator, the latter one is much easier to apply because of its closed-form expression for K-factor. Its utility has been validated with measured data from outdoor fixed wireless channels [15]. In [16], the statistical properties of these two moment-based estimators are compared using asymptotic analysis and simulation. It is shown that there is a tradeoff between the computational simplicity and the statistical efficiency of these two estimators. The first- and second-order moments-based estimator can obtain more accurate estimates given the same sample size, whereas the second- and fourth-order moments-based estimator achieves significant computational simplicity. It is known that for large sample size N, the bias and variance of a moment-based estimator are both proportional to $1/N$ [17]. This tells us that if we collect enough measured samples in practice, both estimators will provide reliable estimation of K-factor. Therefore, in this thesis project, we adopt Greenstein and Michelson's approach to estimating Rician K-factor because of its good compromise

between computational convenience and statistical efficiency.

The rest of this chapter is organized as follows. In Section 2.2, we introduce the moment-based algorithm [15] that will be used to estimate Rician K-factor from a finite number of measured power samples in Chapter 3. In Section 2.3, we describe the simulation methodology for assessing the manner in which accuracy of K-factor estimation is affected by the total sample size and sampling frequency (or correlation between successive samples). In Section 2.4, we present the simulation results that will be used to help us plan the measurement campaign in the following chapter.

2.2   Moment-Based Estimation for Rician K-factor

In [15], a moment-based Rician K-factor estimation algorithm was developed and validated. In this section, we briefly introduce this estimation approach.

The complex signal gain of a fixed wireless channel can be modeled as a frequency-flat response

$$g(t) = V + v(t) \tag{2.3}$$

where V is a complex number and $v(t)$ is a complex zero-mean random time variation caused by people or equipment moving in an indoor environment. This description applies to a particular frequency segment which is smaller than the correlation bandwidth of the channel. In this thesis work, the applied signal will be a single tone, *i.e.*, continuous wave (CW), signal which makes the description applicable for our scenario.

To estimate the Rician K-factor, this frequency-flat response need to be expressed in terms of two moments that can be derived from measured power samples versus time. We denote the corresponding power gain as G which is equal to $|g(t)|^2$, and its time average is

$$G_a = |V|^2 + \overline{|v(t)|^2} + \overline{2Re\left(Vv^*\left(t\right)\right)} \tag{2.4}$$

Since $v(t)$ is a complex zero-mean random process, the last term reduces to zero. By defining new variable $\sigma^2 \equiv \overline{|v(t)|^2}$, Eqn. 2.4 can be rewritten as

$$G_a = |V|^2 + \sigma^2 \tag{2.5}$$

Also we define the value of Root Mean Square (RMS) fluctuation of the power gain G about G_a as

$$G_v = \left[\overline{(G - G_a)^2}\right]^{1/2} \tag{2.6}$$

Given the assumption that $v(t)$ is zero-mean complex random process, it is shown that G_v can be represented as

$$G_v = \left[\sigma^4 + 2|V|^2\sigma^2\right]^{1/2} \tag{2.7}$$

Combining Eqn. 2.5 and 2.7, we can determine the quantities of $|V|^2$ and σ^2 in terms of the second moment G_a and the forth moment G_v^2. Then the expression of Rician K-factor can be obtained by definition of K-factor as it follows

$$K \equiv \frac{|V|^2}{\sigma^2} = \frac{[G_a^2 - G_v^2]^{1/2}}{G_a - [G_a^2 - G_v^2]^{1/2}} \tag{2.8}$$

Now, given K-factor and average measured power gain G_a, the Rician envelope distribution can be determined sufficiently by Eqn. 2.2.

2.3   Simulation Methodology

To plan reliable field measurement campaigns and to apply Rician K-factor estimators in operational systems, we not only need to assess how many measured samples are necessary to be collected for achieving an accurate estimation of K-factor, but also need to be aware of the manner in which accuracy of K-factor estimation is af-

fected by correlation between successive samples. Such correlation will increase as the sampling interval becomes shorter. Here, we employ a computer simulation approach to study the relationship between the accuracy of K-factor estimation, sample interval, and total sample size. In Section 2.3.1, we show how Doppler spread affects the correlation between successive signal samples and briefly describe how we obtain the Doppler spread information used in the following simulations. In Section 2.3.2, we describe a Rician fading envelope generator, while in Section 2.3.3, we give the detailed simulation procedure.

2.3.1 Correlation Between Adjacent Signal Samples

In general, the correlation between the successive samples is directly related to the Doppler spread. If the Doppler spread is small, the channel changes slowly and a high correlation between successive samples can be observed [16]. Thus in order to evaluate the effect of correlated samples on K-factor estimation and simulate correlated Rician fading samples, we first need to study the Doppler spectrum in indoor fixed wireless environments.

As introduced in Chapter 1, there are two types of propagation channels. The first type is often found in the scenario which the transmitter (or receiver) is fixed while the other is in motion. The Doppler spectrum in this type of channel has been extensively investigated. Assuming a uniformly distributed AoA leads to the well-known U-shape spectrum of Clarke [18]. However the U-shape spectrum are not applicable to the fixed wireless channel, where the Doppler spectrum is due to the movement of surrounding objects. Experimental investigations [19, 20, 21] and theoretical analysis [22] show that the the Doppler spectrum for such fixed wireless environments will generally have a peaky shape centred around the carrier frequency.

In order to introduce actual correlation between the samples, actual Doppler spectrum information must be incorporated into the simulation of Rician fading envelopes.

For achieving such spectral information, we took field measurements in 4th floor hall-way of the MacLeod building and obtained 40 time series of measured power samples by varying 20 different locations (two measurement data sets collected for each location). Then, the Doppler spectrum information was extracted from the measured data by employing the Doppler spectrum estimation method in [19], which has been validated by measurement results from fixed wireless environments. Different from most classical estimation methods based on the complex signal's power spectrum, this estimation approach is based on the measured power samples without any phase information.

In this chapter, we will focus on the spectrum estimation results. The detailed measurement campaign and spectrum estimation method will be presented in the Section 3.2 and 3.3 respectively. Figure 2.3 shows the maximum Doppler spectrum (the Doppler Spectrum with maximum width) estimated from the 40 measurement data sets for 20 different locations in the 4th floor hallway of MacLeod building. By taking the linear average of the 40 estimated spectra, we obtain the average Doppler spectrum, as shown in Figure 2.4. Note that all the spectra are normalized so that their maximum value is 0 dB. From these results we can see that our estimated Doppler spectrum also has a peaky shape centred around the carrier frequency, which is consistent with the spectra presented in [19, 20, 21, 22]. Given the estimated Doppler spectrum, we are now able to design the Doppler filter that will be used in the Rician fading envelope generator for introducing correlation between successive samples. The steps for designing the Doppler filter are detailed in Section 2.3.2.

2.3.2 Generation of the Rician Fading Envelope

In the literature, there have been a number of different algorithms proposed for the generation of correlated Rayleigh or Rician random variates. In [23], Young *et al.* presents a quantitative evaluation of three generation methods, specifically, the IDFT

method [24], filtered white Gaussian noise (WGN) method [25] and the superposition of sinusoids method [18]. Comparison shows that the IDFT method to be the most efficient and offers the best quality among the three approaches. Thus, in this thesis work, we use the IDFT algorithm to simulate Rayleigh fading signals and, in a straightforward way, use the result to generate Rician fading envelopes.
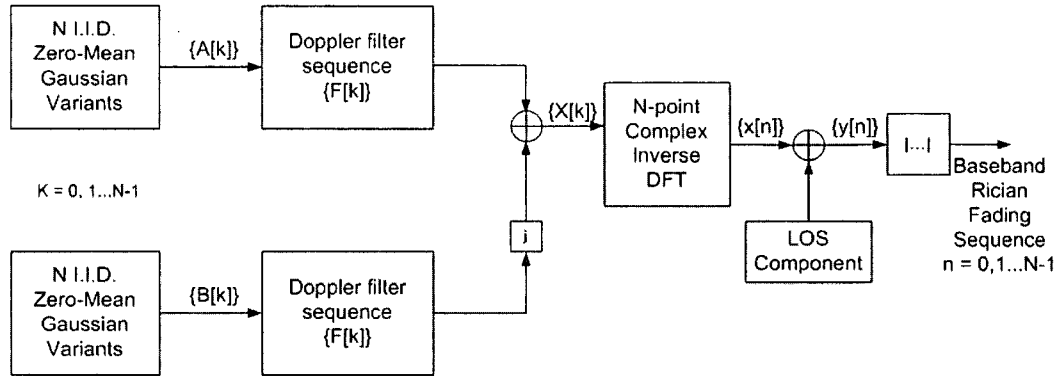
Figure 2.2: Block diagram of the Rician fading envelope simulator

Figure 2.2 shows the structure of the Rician fading envelope simulator. First, two independent zero-mean Gaussian noise sources, $A[k]$ and $B[k]$, are generated. Each is then applied to the Doppler filter $F[k]$. The memory in the filter causes successive samples of the output to be correlated with each other. The two filtered outputs are then combined to form a complex sequence $X[k]$. By applying IDFT to $X[k]$, we obtain a time domain complex sequence $x[n]$, that will have a Rayleigh distributed envelope. In order to achieve a Rician fading envelope, a LOS component is added to $x[n]$ at the final stage of the simulator. Note that the added LOS component is a DC component and implemented by an absolute value without phase information. The detailed procedure to implement the Rician envelope simulator is described in [24].

As described above, the Doppler filter $F[k]$ is used as a spectral shaping filter that introduces the desired amount of correlation into the complex Gaussian sequence. The design of the filter coefficients is based on the estimated spectral results presented

in Section 2.3.1. Here, we use a curve fitting tool in MATLAB to fit the resulting spectrum shown in Figure 2.4 into a rational function, which is plotted in Figure 2.5. Then, given the rational function coefficients, we may define the Doppler filter coefficients according to the approach presented in [24].

Figure 2.6 gives examples of measured and simulated fading envelopes. From this plot, it can be seen that successive signal samples are correlated with each other in both the measured and simulated envelopes.

2.3.3 Simulations over Sampling Frequency and Sample Size

The impact of correlated signal samples on the performance of Rician K-factor estimators was reported by computer simulation methods in [16]. The authors suggest that significant correlation among samples will be introduced when the channel changes slowly (small Doppler spread), and as a direct result, the estimator's performance deteriorates due to the decrease in the total number of independent samples. In addition, their simulation results show that the sample size is also a critical factor that can determine the estimation accuracy.

In general, the smaller the sampling frequency and the larger the sample size, the more accurately K-factor can be estimated. However this will lead to much longer measurement time in practice. Thus in order to achieve accurate estimation of K-factor from a finite length of samples within a reasonable measurement time, a proper sampling frequency and sample size must be carefully chosen for our measurement campaign.

In this chapter, the results of simulation studies designed to investigate the impact of sampling frequency and sample size on the effectiveness of K-factor estimator are presented. The simulation procedure can be divided into the following steps:

1. Given fixed K-factor and mean power, use the Rician fading envelope generator
   to construct 500 correlated Rician fading time series with a certain sampling

frequency and sample size.

2. Apply the Rician distributed sequences to the Rician K-factor estimator introduced in Section 2.2 to obtain 500 estimated K-factors denoted as $\hat{K}_i$.

3. Based on the 500 estimated values of K-factor, perform statistical analysis to obtain the following parameters:

   - Mean: $\mu_k = \frac{1}{500} \sum_1^{500} \hat{K}_i$
   - Standard deviation: $\sigma_k = \sqrt{\frac{1}{500} \sum_1^{500} \hat{K}_i^2 - \left(\frac{1}{500} \sum_1^{500} \hat{K}_i\right)^2}$
   - Root mean square error (RMSE) of estimation about the given K-factor: $RMSE_k = \frac{1}{500} \sum_1^{500} (\hat{K}_i - K)^2$

4. Change the K-factor, sampling frequency or sample size respectively, then repeat the previous three steps.

2.4 Simulation Results

This simulation study is based upon two assumptions. First, we assume that the Doppler spectrum for indoor fixed wireless channels has the peaky shape shown in Figure 2.5. The other assumption, which is based upon observation, is that the frequency components corresponding to frequencies greater than 5 Hz are below -30 dB. Thus, we assume that all the power in the spectrum is contained within the frequency range from -5 Hz to 5 Hz, *i.e.*, the maximum Doppler spread f_d is 5 Hz. In reality, the real measurement of Doppler spectrum will be never reach zero.

First, we ran simulations for determining how many samples we will need to achieve accurate estimation of K-factor given a fixed sampling frequency. We set the sampling frequency f_s equal to $2f_d$ for our first round of simulation. Figure 2.7 shows the RMSE of K-factor estimation as functions of different values of K-factor. We can see that the estimation RMSE decreases as the sample size increases, while the RMSE

increases as the value of K-factor increases. Similar results can also be found in [16]. Another observation is that, when the sample size is over $2^{14}(= 16384)$, the RMSEs for all the simulated K values drop below 0.4. Note, in these simulation studies, we only consider the scenario that K-factor is below 10, in which the relative advantage of space diversity is greater than the scenario that K-factor is above 10.

After determining the numerical relationship between estimation error and sample size, our next step was to study the relationship between estimation error and sampling frequency. Now we choose the K-factor equal to 10, which results in the largest error in our simulation, then investigate the effect of sampling frequency on the estimation accuracy. From Figure 2.8, we can see that the estimation error increases almost linearly as f_s increases. This is because that larger sampling frequency will compress the time interval between two adjacent samples. This shorter time interval will most likely introduce higher correlation between the samples, consequently, the estimation error will increase with the sampling frequency.

2.5 Summary

We have presented simulation results that give the sample duration required to accurately estimate path gain and Rician K-factor given the parameters of the Doppler spectrum (type and cut-off) and the sample rate. This is a useful result for those planning measurement campaigns in indoor fixed wireless environment.
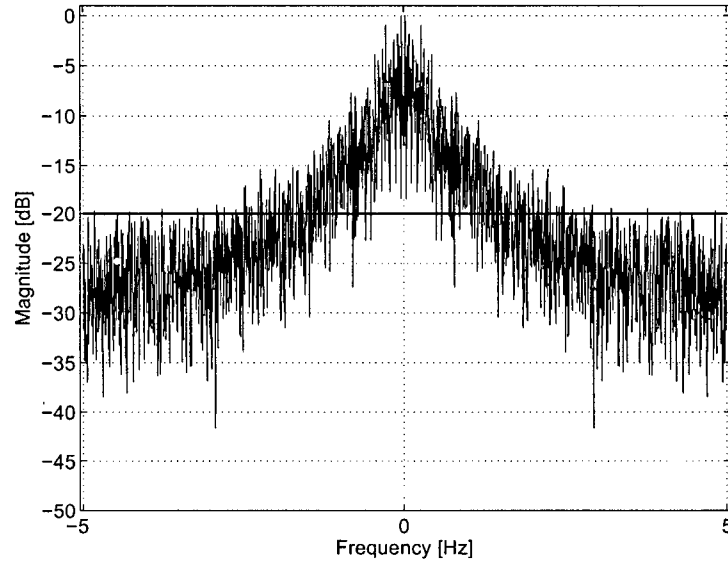
Figure 2.3: Maximum Doppler spectrum observed in hallway of MacLeod 4th floor
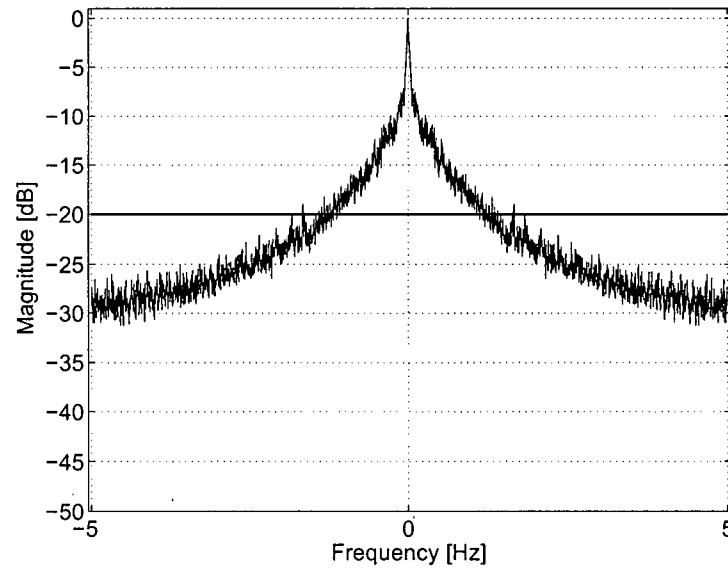
Figure 2.4: Average Doppler spectrum observed in hallway of MacLeod 4th floor
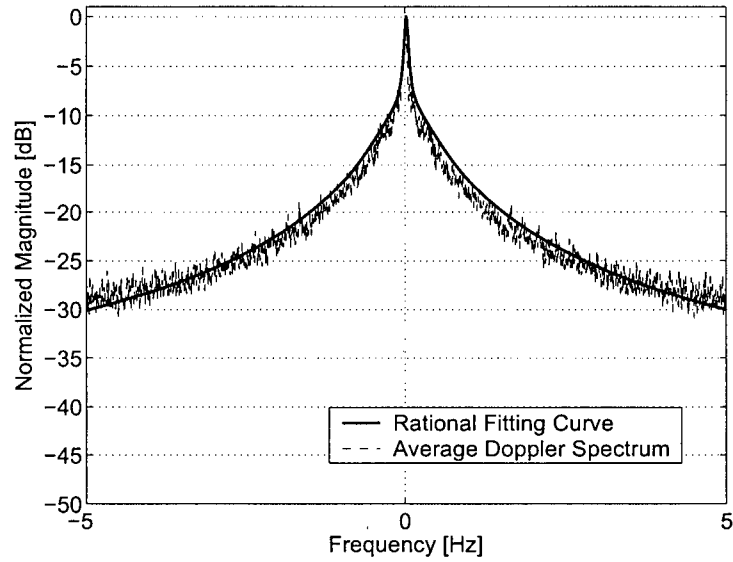
Figure 2.5: Average Doppler spectrum and its rational curve fitting function
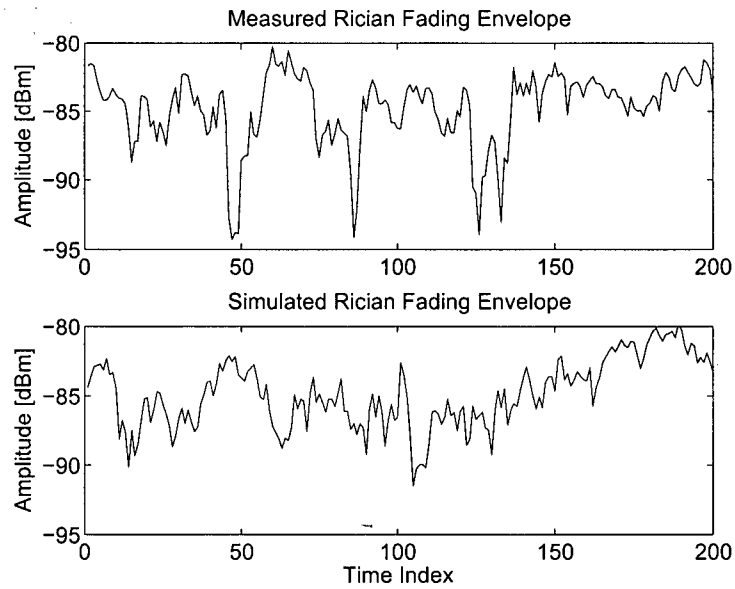

Figure 2.6: Simulated and measured Rician fading envelopes
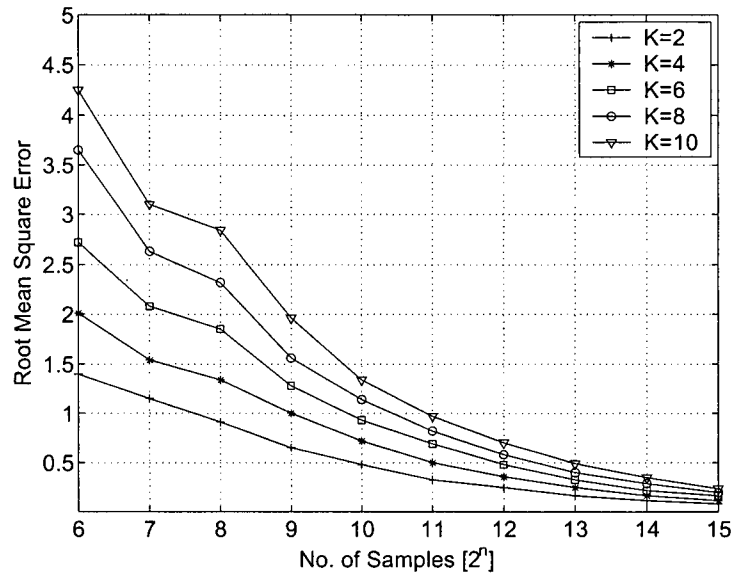
Figure 2.7: Sample size vs. K-factor estimation RMSE (When $fs = 2f_d$)
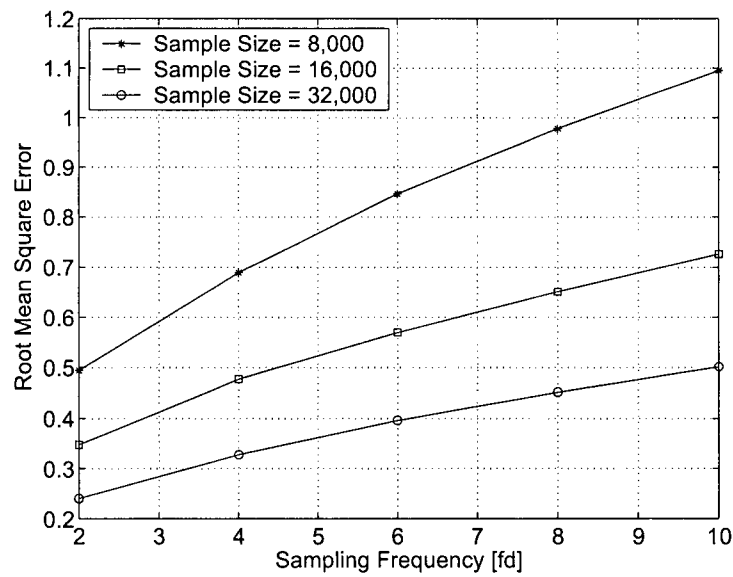
Figure 2.8: Sampling frequency vs. K-factor estimation RMSE (When K = 10)

Chapter 3

Characterization of Indoor Fixed Wireless Channels

3.1 Introduction

The indoor fixed wireless environment is characterized by a transmitter and receiver that are both stationary but scatterers that may be moving. If there is no significant motion in the environment, time variation in the channel is negligible. However, in practical situations, movement of people along the path between the transmitter and receiver is commonly observed. Such body shadowing may result in severe fading.

In the literature, several researchers have addressed different aspects of indoor fixed wireless channels. The fading statistics of the received signal envelope for CW signals in various indoor environments have been measured by various researchers [26, 27, 28, 29]. Hashemi *et al.* [29] measured the fading envelope in office environments in which there was significant people movement and showed that the received envelopes may variously follow Weibull, Nakagami, Rician, Lognormal or Rayleigh distributions. Extensive CW measurements near 1 GHz in office buildings [26, 27] and factory environments [28] have shown that even in the absence of a direct LOS path between the transmitter and receiver, the measured fading envelope shows a good fit to the Rician distribution.

Most previous efforts to characterize the fixed wireless Doppler spectrum are for outdoor channels [19, 20, 22]. Comparatively few studies have been done for indoor scenarios. Howard *et al.* [21] studied Doppler spread in indoor radio environments at

910 MHz, but they only give the Doppler spread ranges between 1.9 and 6.1 Hz, not specific shapes that describe the whole spectrum.

Short range wireless systems commonly use space diversity as an effective technique for mitigating severe fading. In [7, 8], some experiments were conducted to evaluate the merits of space diversity in indoor environments, but their data collection efforts focused on mobile users. In [2, 9], the authors used ray-tracing techniques to simulate space diversity performance in highly simplified representations of indoor radio environments.

The effectiveness of space diversity in body-shadowed indoor environments has not been specifically addressed in previous work. Here, our objective is to use narrowband channel measurement techniques at 2.4 GHz to characterize the CDF, Doppler spreads and spatial correlation of received signal envelopes in such cases.

The remainder of this chapter is organized as follows. In Section 3.2, we describe the details of our measurement campaign including the measurement platform, details of the environment, and the data collection procedure. In Section 3.3, we describe the data post-processing approaches used to estimate the channel characteristics of interest. In Section 3.4, we present our measured results for the first-order statistics of the fading envelope, the Doppler spectrum, and the spatial correlation.

3.2 Measurement Campaign

A block diagram of the measurement platform used to conduct the narrowband measurement is shown in Figure 3.1.

3.2.1 Measurement Platform

The transmitter is shown in Figure 3.2. It is a signal generator (Marconi Signal Generator 2031) connected to a dipole antenna (Cisco AIR-ANT4941). We use it to transmit CW (unmodulated) signals in the 2.4 GHz ISM band. The output power
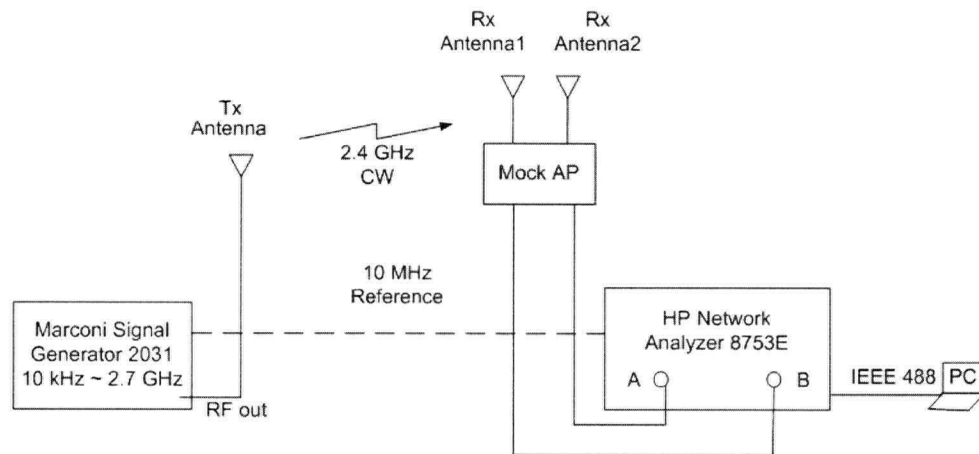
Figure 3.1: The block diagram of narrowband measurement platform

can be set in the range from -144 to +13 dBm. The signal generator also provides a 10 MHz reference signal that can be applied to the receiver for synchronization purpose. The transmitting antenna is a vertically polarized omnidirectional dipole antenna with 2.0 dBi gain. Figure 3.3 shows the antenna's dimensions and its vertical radiation pattern.
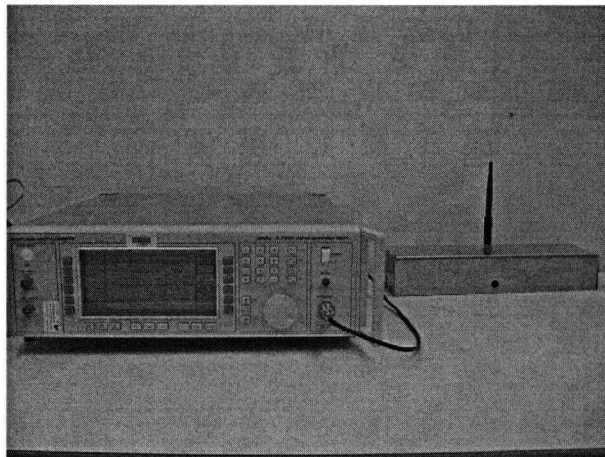
Figure 3.2: Signal generator (Marconi 2031) and transmitting antenna (Cisco AIR-ANT4941)

The receiver is comprised of a mock access point with two receiving antennas
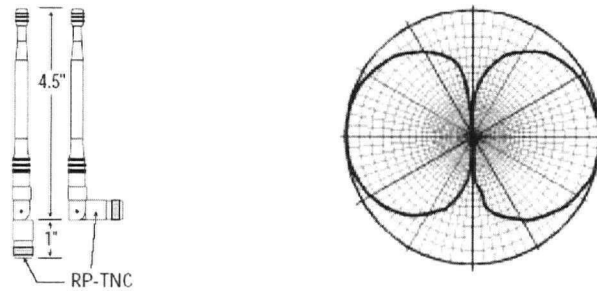
Figure 3.3: Antenna's dimensions and vertical radiation pattern (Source: Cisco Aironet Antenna Reference Guide)

(Cisco AIR-ANT4941), a Vector Network Analyzer (HP 8753E) with the S-parameter test set removed, and a laptop computer with a GPIB interface (NI GPIB-ENET), as shown in Figure 3.4.
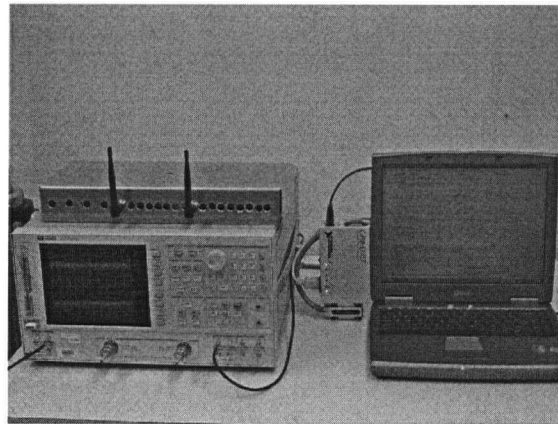
Figure 3.4: Vector network analyzer (HP 8753E), mock AP with receiving antennas (AIR-ANT4941) and GPIB-ENET box

In this narrowband channel sounder, the HP 8753E network analyzer is configured as a dual-channel tuned receiver. It is used to simultaneously measure the power of the received signals applied to ports A and B. For correct operation in this mode, the 10 MHz reference signal from the transmitter must be applied to the reference

input of the network analyzer. A mock access point box with dimensions similar to an actual Bluetooth or WLAN access point was constructed. Provision was made to mount the two receiving antennas at eight different spacings ranging from $\lambda/8$ to λ (1.56 cm to 12.5 cm at 2.4 GHz). The network analyzer is remotely controlled by a laptop via a GPIB-enabled instrument control program.

3.2.2 Description of the Environment

Indoor fixed wireless environments are typically filled with man-made scatterers, *e.g.*, furniture, computers or room dividers. In this type of environment, multipath disturbances and fading effects are often caused by motion of people or equipment in the vicinity of transmitter or receiver.

The measurement campaign was conducted within the MacLeod building on the UBC campus. At the outset, several rooms were identified as potential measurement locations and are listed in Table 3.1.

Table 3.1: Potential Measurement Locations

Type of Environment	Location
Small Office	MacLeod 339
Medium Office	MacLeod 323
Small Classroom	MacLeod 214
Medium Classroom	MacLeod 402
Large Classroom	MacLeod 228
Laboratory	MacLeod 458
Hallway	MacLeod 4th Floor
Lobby	MacLeod Lobby

The main criteria for choosing a measurement site is that at least one diversity branch receives a signal envelope with Rician K-factor lower than 10 within a ten-minute survey run. This means that motion of people may cause an obvious signal variation and severe multipath fading at the site. Ultimately, two sites were chosen to conduct the narrowband measurement campaign: medium office MacLeod 323 and

laboratory MacLeod 458.

MacLeod 323 is a typical medium office environment. It has an area of about 32 square metres and is equipped with desks, chairs, cubicle panels and shelves, as shown in Figure 3.5. Three sides of the room are 10-cm concrete walls. The fourth side is a panel of windows. The ceiling is covered by acoustic tiles and has a height of 3.6 metres. Linoleum tiles cover the concrete floors.
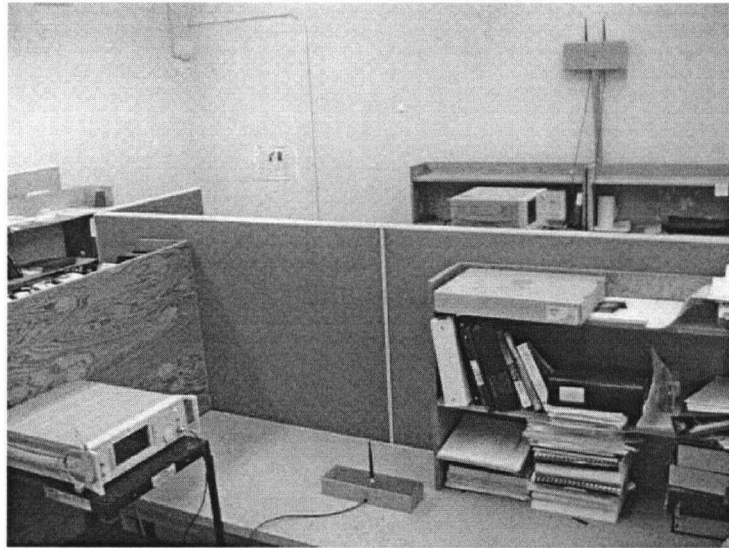
Figure 3.5: Typical medium office environment: MacLeod 323

MacLeod 458 is a typical laboratory environment. It has the same basic construction material and structure as MacLeod 323, but has over three times the area (112 square metres). It is furnished with wooden tables, lab benches and office swivel chairs. A few metal cabinets and wooden bookshelves stand against the walls. Unlike MacLeod 323, the laboratory is full of computers, work stations and electronic equipment, as shown in Figure 3.6. As a result, this environment is a good example of a rich scattering indoor environment.
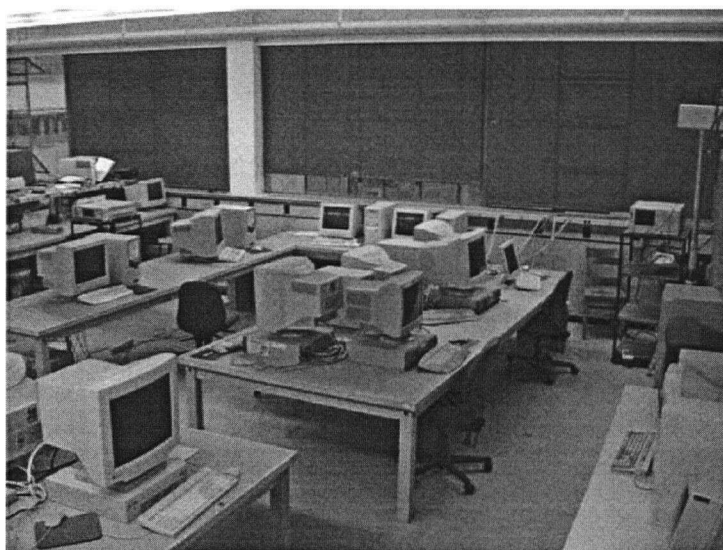
Figure 3.6: Typical laboratory environment: MacLeod 458

3.2.3 Data Collection

At each measurement site, the mock access point and receiver were placed at a specific location in the room. It was not moved again until all measurements in that room were complete. Figure 3.7 and 3.8 shows where the receivers were placed in MacLeod 323 and 458, respectively. In practice, WLAN and Bluetooth access points are often mounted on the walls or directly on the ceiling. In our measurements, we placed the mock access point against the wall at a height of approximately 2.4 metres.

We placed the transmitter in the same room as the receiver so that the AoA could be easily estimated. Before recording a full set of measurement data, 40-second short tests were conducted in order to identify transmitter locations at which at least one branch of received signal experiences severe multipath fading during a certain time segment, as shown in Figure 3.9.

At each site, the transmitter was placed in five locations as shown in Figure 3.7 and 3.8. We ensured that these five points were separated from each other at least a one wavelength. A one-wavelength spacing between each transmitter location
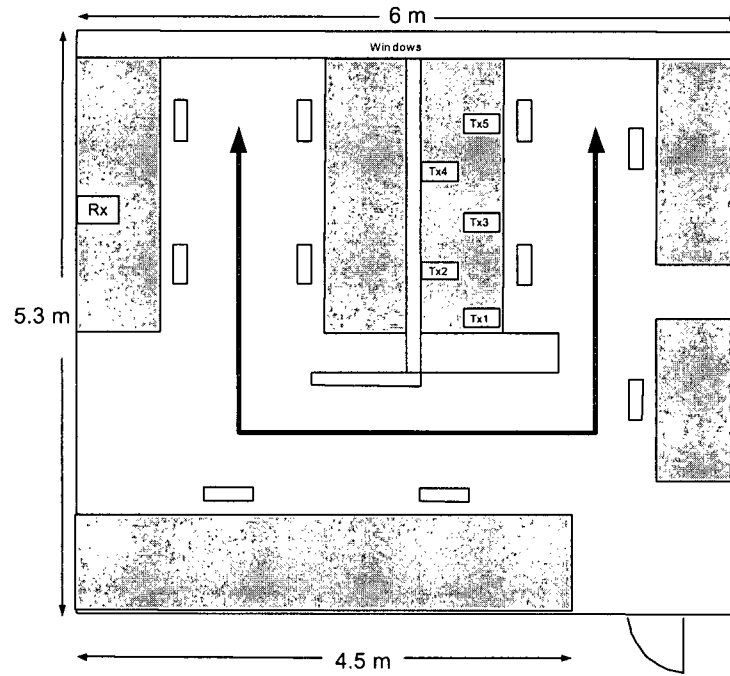
Figure 3.7: Transmitter (Tx) and Receiver (Rx) locations in MacLeod 323
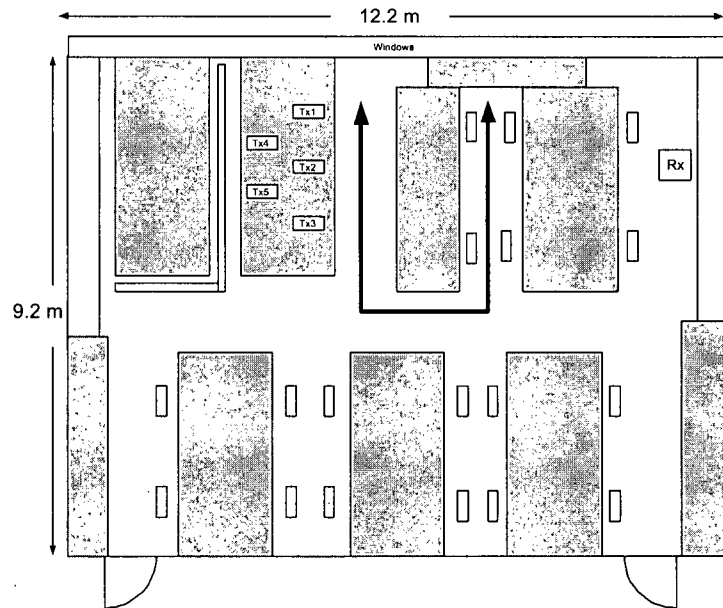

Figure 3.8: Transmitter (Tx) and Receiver (Rx) locations in MacLeod 458
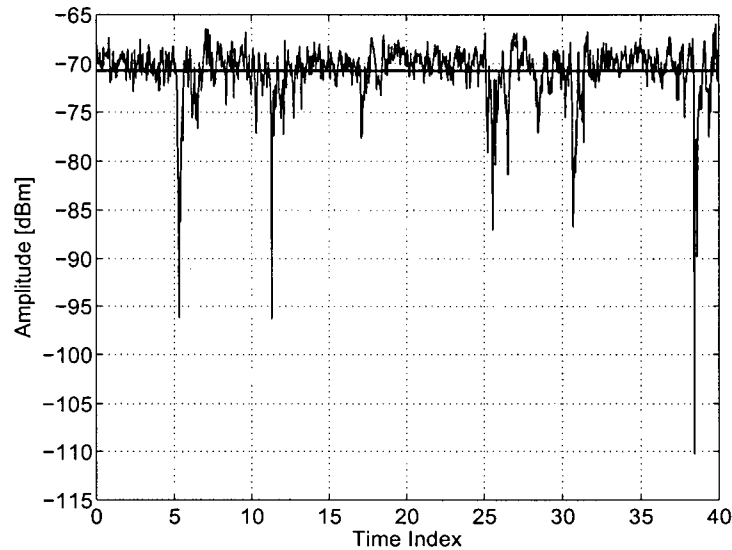
Figure 3.9: Received signal power envelope recorded in MacLeod 458

provides multiple independent observations of the propagation environment. During the measurements, we introduced controlled movement of people at a speed of around 3 km/h between the transmitter and receiver. Figure 3.7 and 3.8 show the paths of the moving people.

Given specific transmitter and receiver locations, the measurement platform can be set up with the measurement parameters listed in Table 3.2.

During each measurement sweep, 1601 data points were collected within 40 seconds, *i.e.*, the sampling frequency is 40 Hz, which is roughly two to four times higher than the maximum Doppler frequency observed in similar cases. We repeat the process ten times in quick succession in order to collect around 16,000 data samples in total. According to the simulation results in Chapter 2, for a Rician K-factor equal to 10, the sample size of 16,000 and sampling frequency of $2f_d$ to $4f_d$ will limit the RMSE to less than 5%, which can be treated as an accurate estimate for our purposes.

The source power level was set to -30 dBm in order to yield a received signal level

Table 3.2: Measurement Parameter Setting

Transmitter	Centre Frequency	2.4 GHz
	Output power	-30 dBm
	Modulation	Unmodulated
	Reference Frequency	10 MHz
	Antenna Height	0.75m
Receiver	Centre Frequency	2.4 GHz
	Mode	Tuned Receiver
	Dual Channel	Yes
	Coupling	Yes
	External Source	10 MHz
	IF Bandwidth	100 Hz
	Points/Sweep	1601
	Sweep Time	40 s
	Number of Sweep	10
	Antenna Height	2.4 m
	Antenna Spacing	0.125λ - 1.0λ

between the range of -60 and -80 dBm, a typical range for received power by short range wireless devices.

3.3 Measurement Data Post-processing

3.3.1 Received Signal Envelope Distributions

We took the measurements using five transmitter locations for each site. For each location, the antenna spacings were varied from 0.125 wavelength to 1.0 wavelength and there were two diversity branches for given specific location and antenna spacing. Thus overall we collected eighty measurement data sets for each measurement site. Each of these measurement data sets contains 16,000 samples of received signal envelope power.

Eighty such data sets were collected at each of the two sites yielding a total of 160 data sets. Before combining the two diversity branches, these data sets were used to determine whether the fading envelopes follow a Rayleigh or Rician distribution.

First, the measured data sets were normalized by subtracting the average received power (on a logarithmic scale). Then the CDF of that data set was calculated, yielding 160 CDFs. In order to determine which distribution is the best fit to the received signal envelopes, the CDFs of measured data were compared to the corresponding Rayleigh and Rician CDFs simultaneously. In each case, we determined the most likely value of the Rician K-factor using the estimator introduced in Chapter 2.

Other distributions, *e.g.,* Nakagami and Weibull distributions, may be more accurate in certain situations [29]. However Rayleigh/Rician are the only ones commonly implemented in RF simulation tools and RF channel emulators. Accordingly, we have chosen to describe the amplitude distribution in terms of the Rayleigh/Rician distribution in this thesis work so that our results may be more easily used in conjunction with such tools.

3.3.2 Doppler Spectrum Estimation

The first step in estimating the Doppler spectrum is to determine the autocorrelation function of the measured power samples. The power samples were converted from logarithmic to linear scales, yielding $p(i)$. We found the mean power $\bar{p}$ and then obtained a set of zero-mean power samples $\bar{p}(i)$ by subtracting the mean power from $p(i)$. From $\bar{p}(i)$, we can estimate the autocorrelation function $A(m)$ of the discrete-time zero-mean power series. If $\overline{K}$ is the estimated Rician K-factor, we can transform the power process autocorrelation function $A(m)$ into the autocorrelation function of the received signal $a(m)$ using

$$a(m) = \sqrt{\overline{K}^2 + A(m)} - \overline{K} \tag{3.1}$$

as described in [19].

The next step is to obtain the Doppler spectrum by taking the Fourier transform

of the autocorrelation function. Because the autocorrelation function $a(m)$ has a finite number of samples, a windowing function needs to be applied to $a(m)$ before we transform it into the frequency domain. Transforming a signal of finite length is equivalent to convolving the corresponding signal of infinite length by the transform of a rectangular pulse of the same width as the sample. This causes ripples to appear in the output spectrum near the edges of frequency band causing spectral distortion. One technique to reduce the ripples is to multiply input signal by a tapered window. The Blackman window is a popular choice because of its high sidelobe suppression capability. This kind of tapered window has the following time domain transfer function, as depicted in Figure 3.10

$$b(m) = 0.42 - 0.5 \cos\left(2\pi \frac{m}{N-1}\right) + 0.08 \cos\left(4\pi \frac{m}{N-1}\right) \tag{3.2}$$

where N is the window length and m is the time index ranging from 0 to N-1.
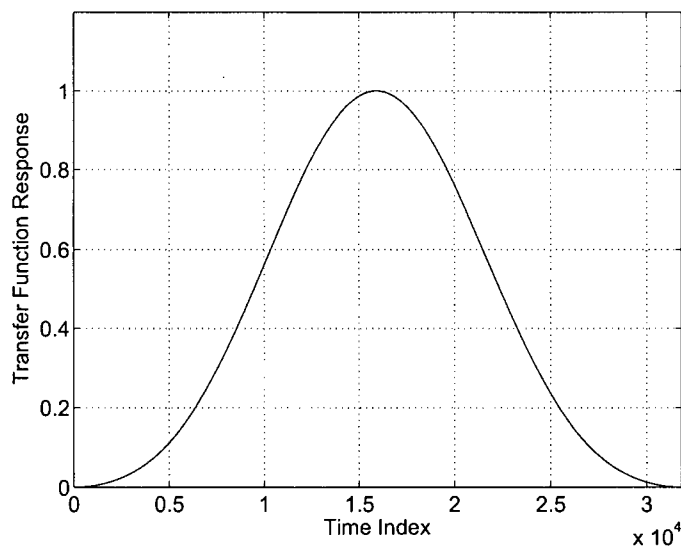
Figure 3.10: Transfer function response of Blackman window

After multiplying the windowing function, we can perform the discrete Fourier

transform on the resulting autocorrelation function $a(m)$ to achieve the Doppler spectrum $S(f)$ as follows:

$$S(f) = \sum_{m=1}^{N} a(m)b(m)e^{-j2\pi fm} \tag{3.3}$$

where all the frequency components of the Doppler spectrum $S(f)$ are limited between $-F_s/2$ and $F_s/2$, where F_s denotes the sampling frequency and is equal to 40 Hz in this work.

3.3.3 Spatial Correlation

There are three different forms of spatial correlation coefficients reported in previous studies: complex signal (ρ_s), envelope (ρ_e), and the power correlation (ρ_p) coefficients [30]. The complex signal correlation coefficient is defined as

$$\rho_s = \frac{E\left[V_1 V_2^*\right]}{\sqrt{E\left[V_1 V_1^*\right] E\left[V_2 V_2^*\right]}} \tag{3.4}$$

where V_1 and V_2 are the zero-mean complex voltages at the receiving antenna, and $E\left[\cdot\right]$ is the expected value operator. The definition of the envelope and power correlation coefficients are as follows:

$$\rho_e = \frac{E\left[\sqrt{P_1}\sqrt{P_2}\right]}{\sqrt{E\left[\sqrt{P_1}\sqrt{P_2}\right] E\left[\sqrt{P_1}\sqrt{P_2}\right]}} \tag{3.5}$$

$$\rho_p = \frac{E\left[P_1 P_2\right]}{\sqrt{E\left[P_1 P_2\right] E\left[P_1 P_2\right]}} \tag{3.6}$$

where P_n is the zero-mean received signal power over the nth antenna. In this thesis, the power correlation coefficient is used, because it will make our spatial correlation results comparable with the theoretical results Eqn. 1.1.

As described previously, the measurement results recorded by network analyzer are absolute values of power with units of dBm. Thus before we calculate the spatial

correlation, it is necessary to transform the logarithmic values of measured power sample $P_n[i]$ into linear values $p_n[i]$, where $P_n[i]$ logarithmic values of measured data with time index i and $p_n[i]$ are the linear values with units of milliwatts. For simplicity, in the rest of the thesis we use ρ to denote the values of the power correlation coefficient ρ_p, so the spatial correlation can be represented as

$$\rho = \frac{\sum_{i=1}^{N}(p_1[i] - \bar{p_1})(p_2[i] - \bar{p_2})}{\sqrt{\left(\sum_{i=1}^{N}(p_1[i] - \bar{p_1})^2\right)\left(\sum_{i=1}^{N}(p_2[i] - \bar{p_2})^2\right)}} \quad (3.7)$$

where $\bar{p_n}$ is the average value $p_n[i]$ and N is the total number of samples recorded during each measurement.

3.4 Measurement Results

Fading Envelope Distribution

An example of the received signal envelope for the indoor fixed wireless measurements is shown in Figure 3.11. Instances of severe fading caused by both direct blockage and destructive interference (phase cancellation) when people moving around are apparent.

The CDFs of all the measured data were calculated and compared to the corresponding Rayleigh and Rician CDFs. In all cases, a Rician distribution offers a far better fit than the Rayleigh distribution. As an example of the Rician fading behavior, Figure 3.12 shows a CDF of the normalized measured envelope based upon measurement data collected in MacLeod 323. The estimated Rician K-factor is 4.2, which is a typical medium value of K-factor observed in the fixed wireless measurements. Figure 3.13 shows the CDF of the received fading envelope based upon measurement data collected in MacLeod 458. Here, the estimated Rician K-factor is 16.
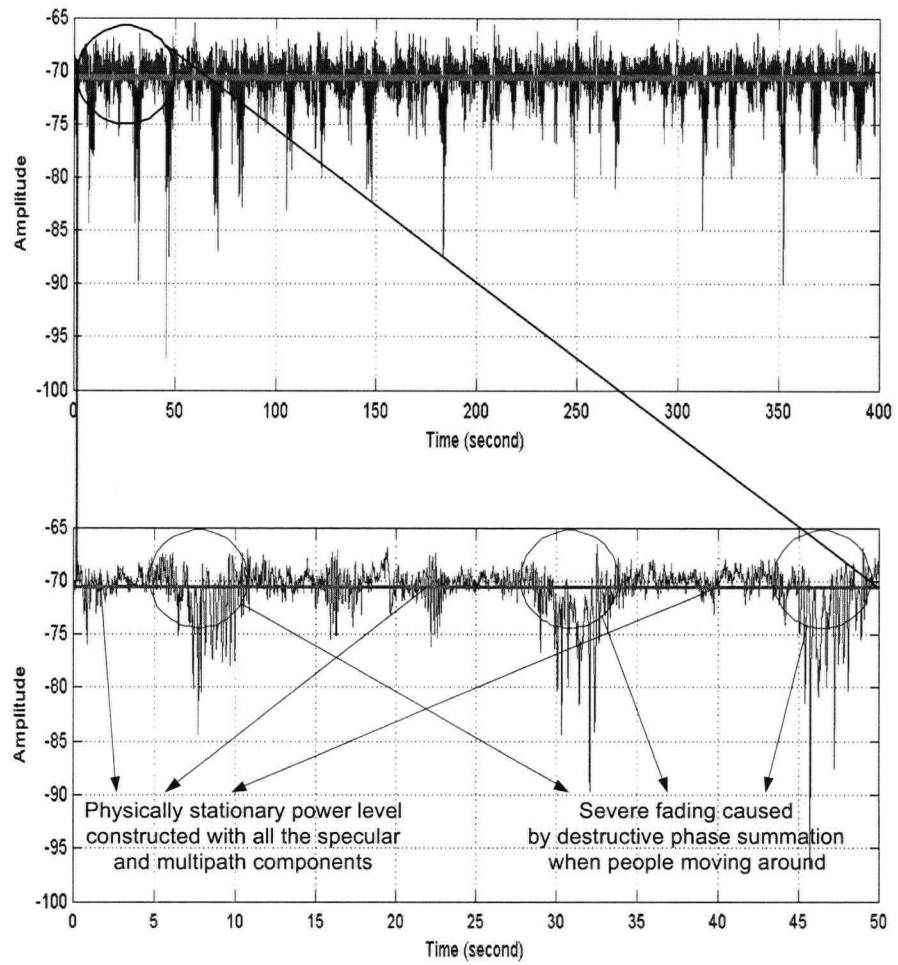
Figure 3.11: An example of the received signal envelope for the indoor fixed wireless environments

Doppler Spectrum

In the literature, experimental observations of Doppler spectrum in either outdoor or indoor fixed wireless environments were reported by [19, 20, 21] and others. All of the recorded Doppler spectra have a common shape, *i.e.*, a peaky shape centred at the carrier frequency. Although similar results were found when we analyzed the data collected in MacLeod 323, the spectra from MacLeod 458 are quite different.

In Figure 3.14 and 3.15, we plot the minimum and maximum estimated Doppler spectra (respect to spectrum width) based upon eighty data sets collected in MacLeod 323. For the minimum spectrum plot, the width of the spectrum for levels of 5, 10 and 25 dB below the maximum are 0.3, 1 and 10 Hz, while for the maximum spectrum plot, the spectrum width are 1, 1.2 and 13 Hz. We can see from the figures that most of the power is concentrated around the centre frequency and the power density decreases as the frequency increases. Figure 3.16 shows the average of the eighty estimated power spectra in MacLeod 323, which is obtained by averaging all the individual spectra in linear scale. The average spectrum width for levels of -5, -10 and -25 dB are 0.7, 1.5 and 12 Hz respectively. Note that the estimated Doppler spectrum does not keep decreasing as the frequency offset increases. This is mainly due to the noise floor of our measurement equipment which is around -100 dBm. This resulting spectrum is consistent with both the experimental results reported in the literature [19, 20, 21] and theoretical predictions [22].

The estimated minimum, maximum and average Doppler spectra for MacLeod 458 are plotted in Figure 3.17, 3.18 and 3.19. We can see that the average spectrum width for levels of -5, -10 and -25 dB are 0.2, 1.2 and 14 Hz respectively.

The major difference between the average Doppler spectrum shapes in Figure 3.16 and 3.19, are the sidebands near 6.5 Hz that are apparent in the latter. Such sidebands are the result of motion in the environment (a shift of 6.5 Hz corresponds to a velocity of 3 km/h.) and are not completely unexpected, but were not reported by in previous

experimental results or theoretical analysis of the indoor channel [19, 20, 21, 22]. A similar effect has, of course, been reported in Doppler radar studies, *e.g.,* [31].

Spatial Correlation

Figures 3.20 and 3.21 show the spatial correlation coefficient as a function of antenna spacing based upon measurement data collected in MacLeod 323 and 458. These data were collected under the assumption that the AoA of the specular component is broadside to the diversity antennas. In the figures, a theoretical curve is also plotted for illustration purpose and convention. As described in Chapter 1, this theoretical curve is given in the form of zero-order Bessel function as Eqn. 1.2, by assuming Clarke's 2-D isotropic scattering model.

From Figure 3.20, we can see that the measured spatial correlations decrease as the antenna spacing increases. The first lowest value appears around 0.9λ. From this plot, we also can see that almost all the measured correlations are higher than the corresponding theoretical values for a given antenna spacing except for 0.125λ antenna spacing, where the correlations are around 0.65 lower than the theoretical value 0.73. This is likely due to the mutual coupling effect which distorts the two closely spaced antennas' radiation patterns. Compared with the analytical results presented by [5], our measured correlations are much higher. In their work, the spatial correlation which is affected by mutual coupling effect will be around 0.25 for 0.125λ antenna spacing. The main reason for this difference is likely because our measurements are performed in a small enclosed environment in which a very strong direct component exists. The assumption of a uniformly distributed AoA as made by [5] is not valid here. Thus one can expect a higher degree of correlation in our measurement results due to the narrower angle spread. Similar observations can also be found in the correlation results measured in MacLeod 458, which is depicted by Figure 3.21. Three correlation coefficients out of the five have a small negative value

for 0.875λ antenna spacing. This is probably due to effects related to the limited total sample size. It is conceivable that this negative value would become positive if more measured samples were used in the correlation computation. The similar negative power correlation coefficients can also be found in [32].

By linearly averaging the spatial correlation coefficients observed at the five different transmitter positions for given antenna separation, the trend in spatial correlation as a function of antenna spacing in both environments is revealed, as shown in Figure 3.22. We can see that the correlations for all of the antenna spacings are below 0.7, which is typically considered to be low enough for effective diversity reception. As the antenna spacing increases beyond a half wavelength, all the correlations drop below 0.3.
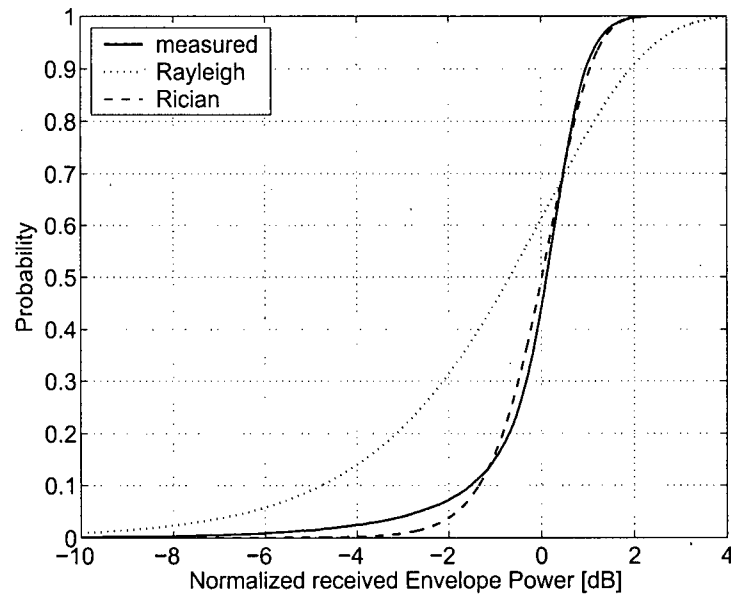
Figure 3.12: The CDF of the normalized received envelope measured in MacLeod 323
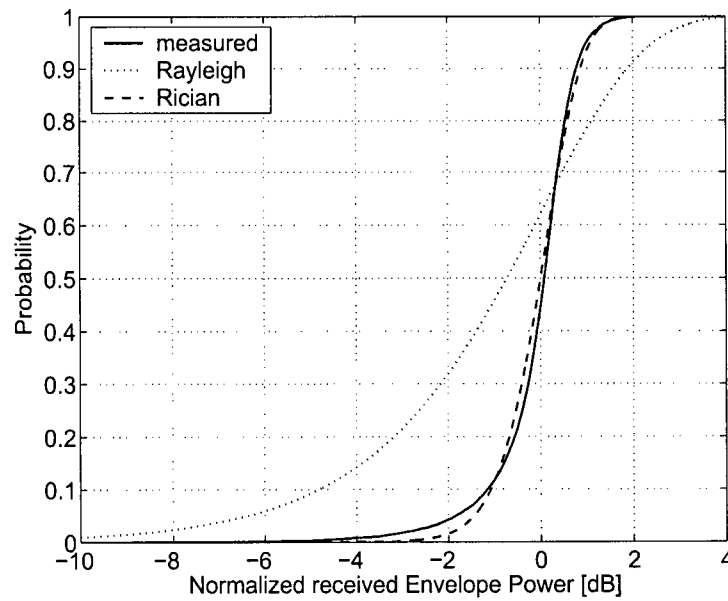
Figure 3.13: The CDF of the normalized received envelope measured in MacLeod 458
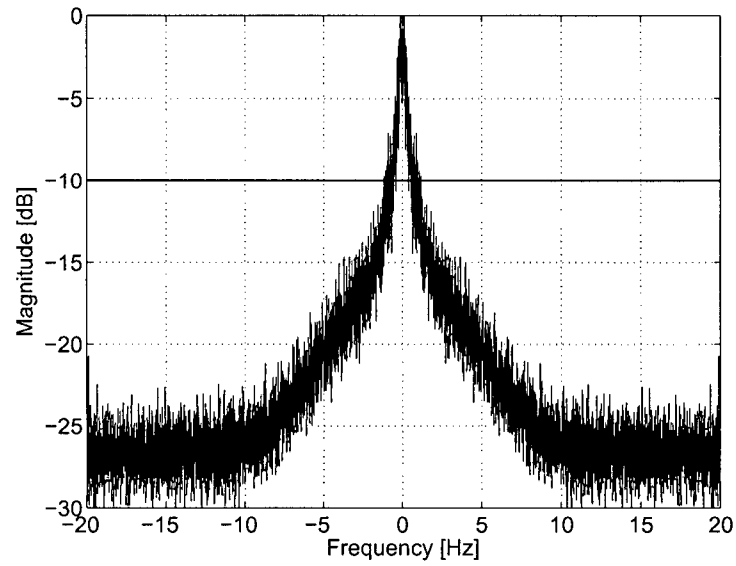
Figure 3.14: The minimum estimated Doppler spectrum for MacLeod 323
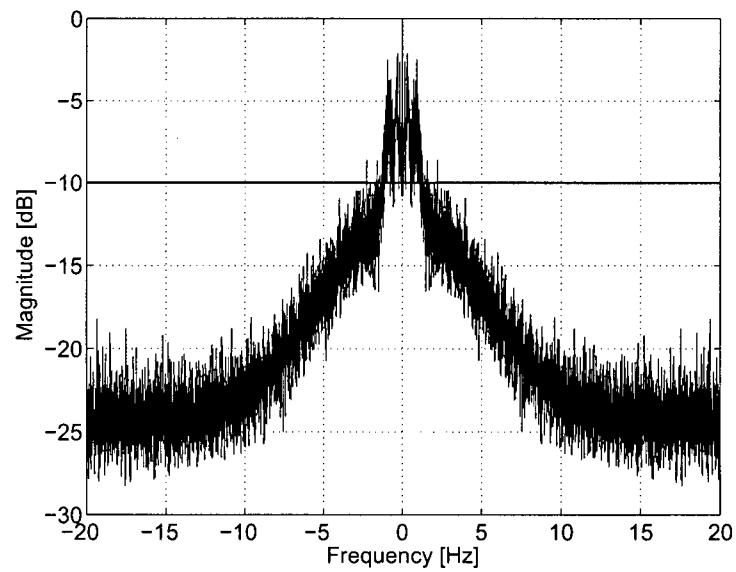
Figure 3.15: The maximum estimated Doppler spectrum for MacLeod 323
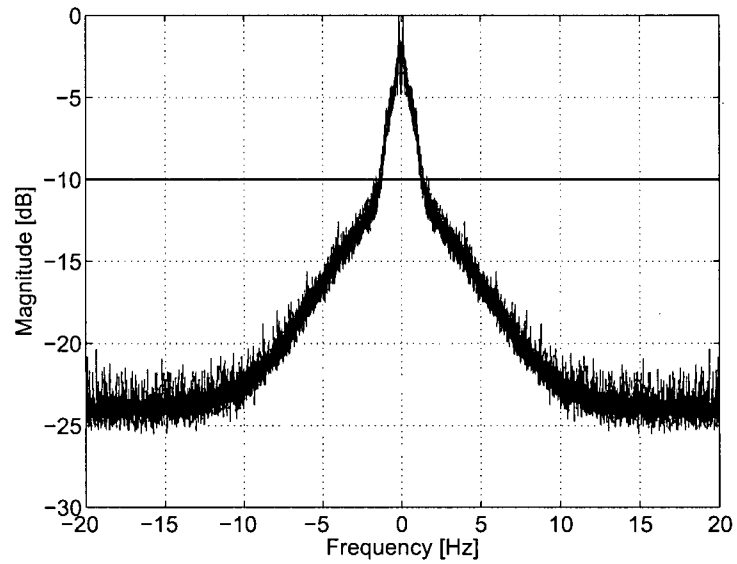
Figure 3.16: The average Doppler spectrum for MacLeod 323
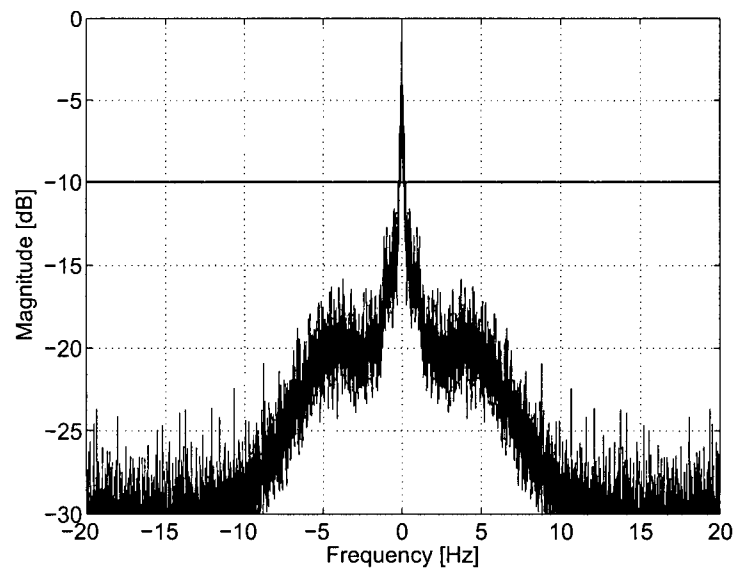
Figure 3.17: The minimum estimated Doppler spectrum for MacLeod 458
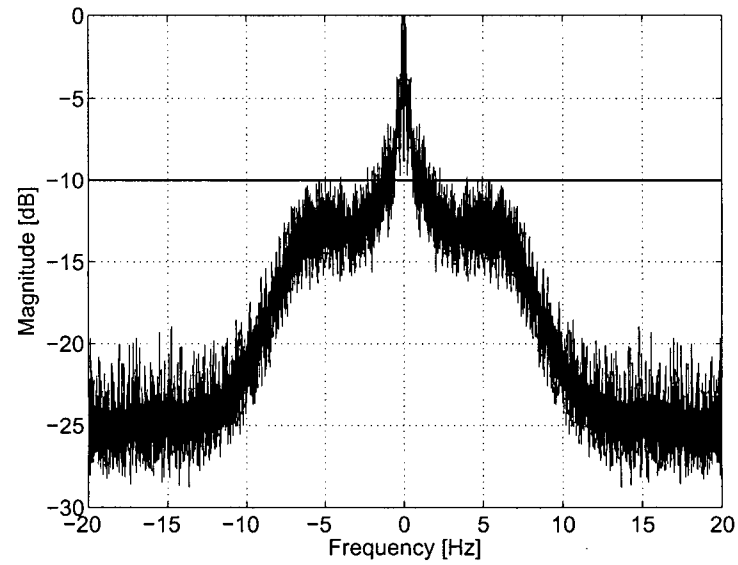
Figure 3.18: The maximum estimated Doppler spectrum for MacLeod 458
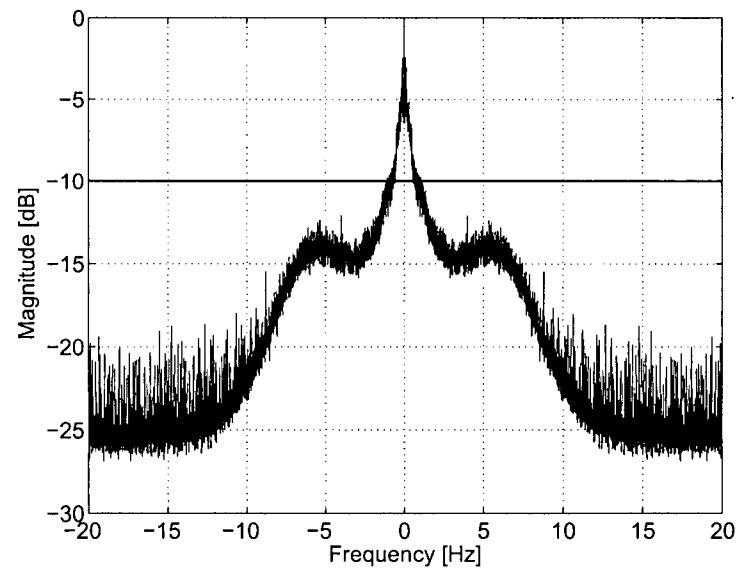
Figure 3.19: The average Doppler spectrum for MacLeod 458
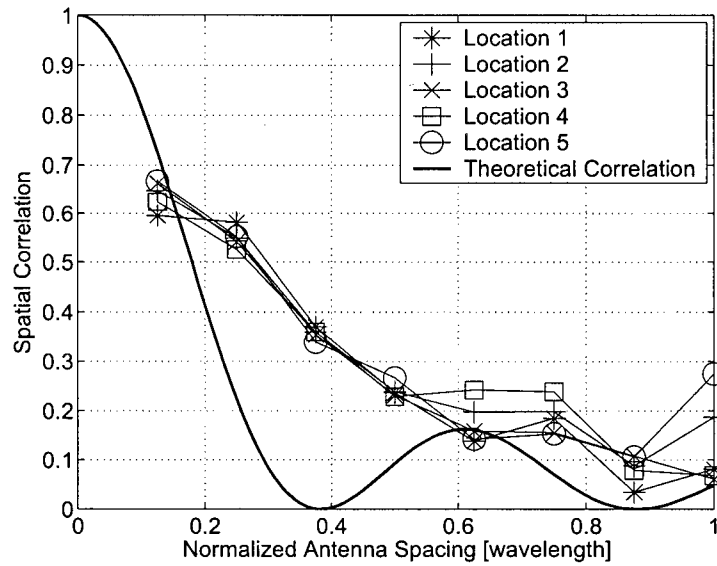
Figure 3.20: The spatial correlation as a function of antenna spacing estimated for MacLeod 323
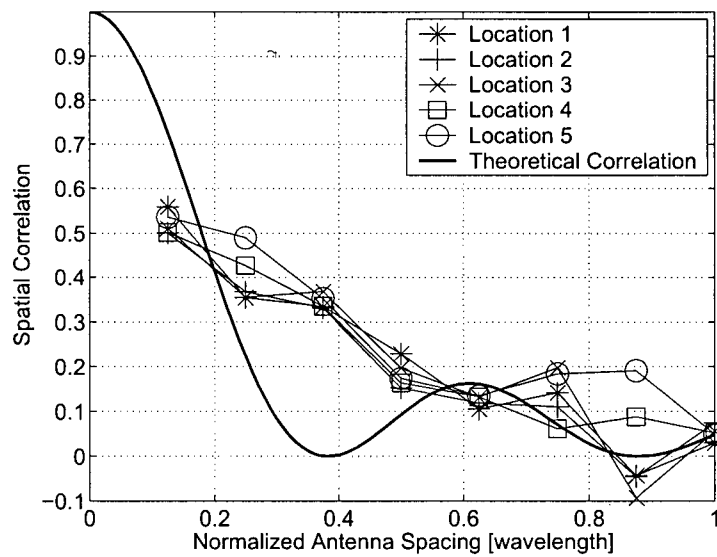
Figure 3.21: The spatial correlation as a function of antenna spacing estimated for MacLeod 458
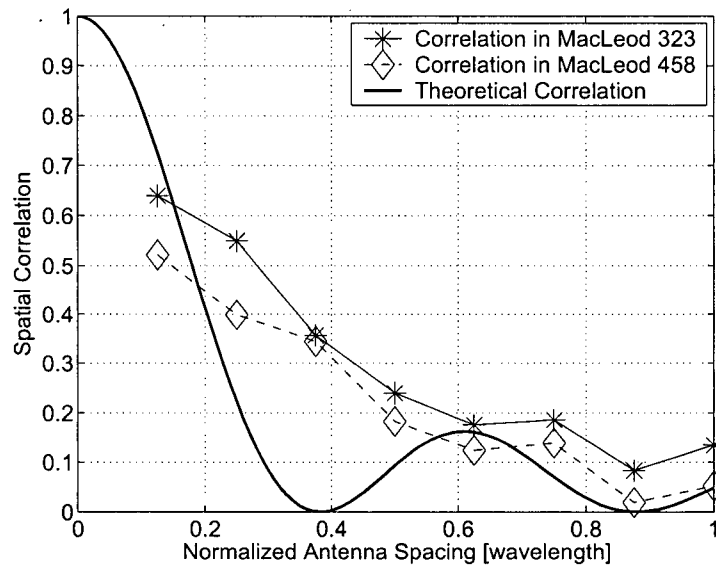
Figure 3.22: Averaged spatial correlation as a function of antenna spacing

3.5 Summary

In this chapter, we have presented measurement results that show the received signal envelope tends to follow the Rician distribution when people move between the transmitter and receiver. We have also revealed details of the manner in which body shadowing affects the shape of the Doppler spectrum observed in indoor fixed environments. In particular, we have shown that body movement can give rise to small sidebands in the Doppler spectrum. Finally, we compared theoretical predictions of spatial correlation as a function of antenna spacing to the measurement results and found reasonable agreement. The results give us confidence that our measurement system is suitable for use in more ambitious measurement campaigns in the future.

Chapter 4

Simulations for Indoor Fixed Wireless Channels

4.1 Introduction

In this chapter, we show how measurement-based models can form the basis for dynamic simulations of space diversity channels in indoor fixed wireless environments. These simulations incorporate the estimated spatial correlation and Doppler spectra presented in Chapter 3 to generate two correlated Rician fading envelopes with known K-factor, which can be treated as an indicator of environment change. We then estimate the diversity gain based on the simulated dual branch signals under the simplifying assumption that the mean signal strength on both branches are identical.

The rest of this chapter is organized as it follows. In Section 4.2, we describe the method used to generate the dual-branch cross-correlated Rician fading envelopes that we used to simulate diversity reception over indoor fixed wireless channels. In Section 4.3, our measurement-based simulation approach is validated by comparing the statistics estimated from measurement and simulation results respectively. In section 4.4, we present the numerical results produced by our measurement-based approach that demonstrates the effectiveness of space diversity in the environment of interest.

4.2 Generation of Dual-branch Cross-correlated Rician Fading Envelopes

The structure used to simulate dual-branch cross-correlated Rician fading envelopes is shown in Figure 4.1. This simulation method is an extension of the IDFT algorithm
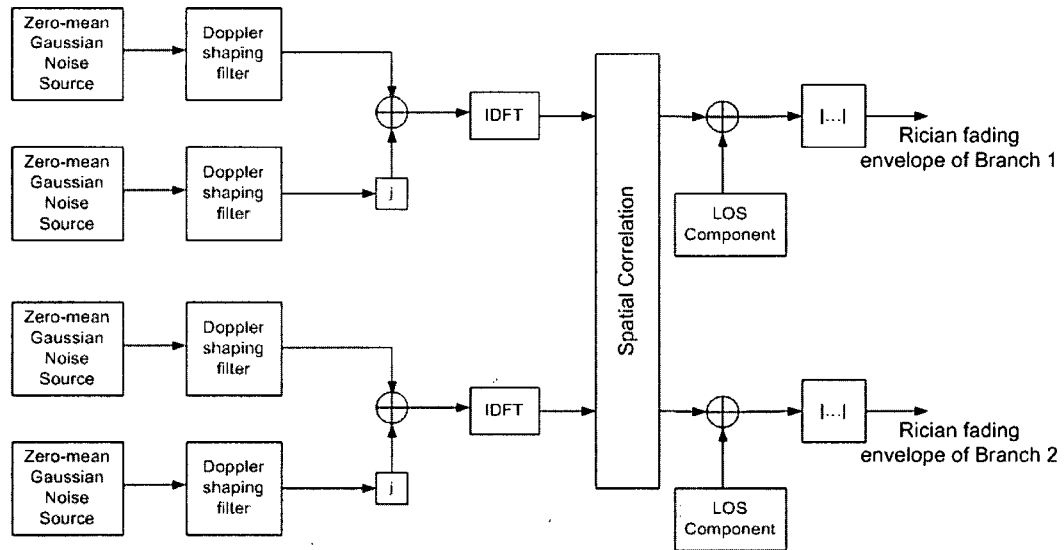
Figure 4.1: The block diagram of simulator of dual-branch cross-correlated Rician fading envelopes

used to simulate Rician fading envelope in Section 2.3.2.

The simulation proceeds as follows:

1. Generate four independent zero-mean real Gaussian sequences.

2. Pass each of the four complex Gaussian sequences to a Doppler shaping filter in order to achieve the desired Doppler spectrum. The coefficients of Doppler shaping filter are determined from the estimated Doppler spectrum depicted in Figure 3.16 or 3.19.

3. Combine two of the filtered Gaussian sequences (which are treated as in-phase and quadrature components respectively), then take inverse Fourier transform

to obtain two independent complex time sequences whose envelopes follow a Rayleigh distribution.

4. In order to introduce cross-correlation into these two simulated envelopes, we adopt the technique in [33], which is a simple numerical method to generate N ($N \geq 2$) correlated Rayleigh fading envelopes with an arbitrary covariance matrix. This is implemented in the spatial correlation function shown in Figure 4.1. Note that the cross-correlation coefficient of complex Gaussian sequences needs to be numerically evaluated such that the resulting Rician fading envelopes are described by the desired covariance matrix.

5. In the final stage, add LOS components, which are determined by Rician K-factor, to the two correlated complex Gaussian sequences. As described in Chapter 2, the LOS components are added as DC components without phase information. Finally, the envelopes of resulting sequences will be Rician distributed with desired cross-correlation coefficient.

4.3 Validation of the Simulation

4.3.1 Signal Envelope Validation

To validate the applicability of our computer simulation methodology, we first compare the single branch of simulated signal envelope with a measured signal envelope.

Figure 4.2 and 4.3 show an example of simulated and measured resulting CDF and Doppler spectrum respectively. In the CDF plot, Figure 4.2, there is a slight difference between the simulated signal envelope CDF with the measured one, which will be more obvious if plotted in logarithm scales. This is mainly due to the imperfect match in the CDF tail region of the experiment results and the theoretical Rician distribution
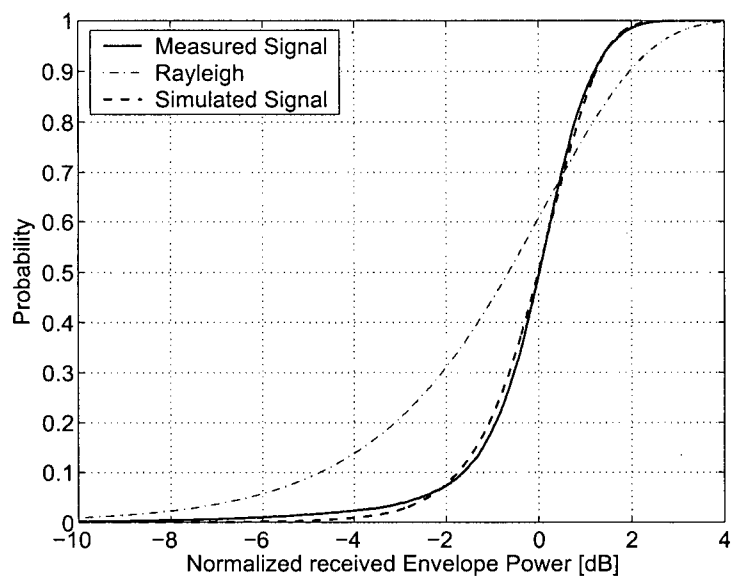
Figure 4.2: The comparison of simulated and measured signal envelope CDF
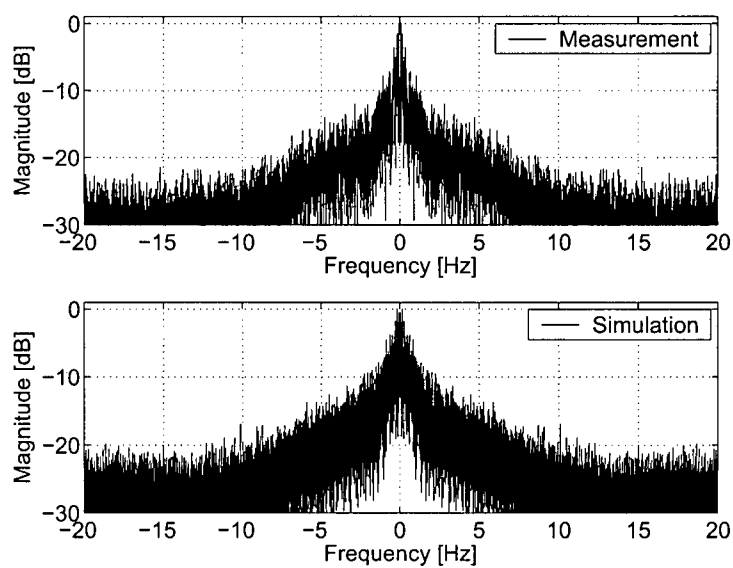
Figure 4.3: The comparison of simulated and measured signal Doppler spectrum

curves. From the Figure 4.3, we can see that the simulated signal envelope preserves the spectral shape and characteristics of the measured signal envelope.

4.3.2 Diversity Gain Validation

Although there are some CDF discrepancies between the simulation and measurement, our main interest is to compare the diversity gain associated with the simulation and measurement results.

Figure 4.4 plots the CDFs of the single and combined branch of signal envelopes for simulation and measurement data. Note that since there are a total of 16,000 samples for each measurement run, we can only obtain reliable statistical characteristics of the order of 10^{-2}. As shown in Figure 4.4, the simulated CDF curves always track the measured CDF curves at the same extent for both single branch signal and combined signal. It suggests that the diversity gains of the simulation and measurement results will be quite similar. The comparison of actual diversity gains is depicted in Figure 4.5. It can be seen that diversity gain estimates from the simulation and measurement results agree closely.

From these validation results, it can be concluded that although there exist some discrepancies in CDFs, our computer simulation can provide a reasonable accuracy of diversity gain estimation. Therefore, the computer simulation methodology can be considered as a reliable approach for space diversity evaluation.
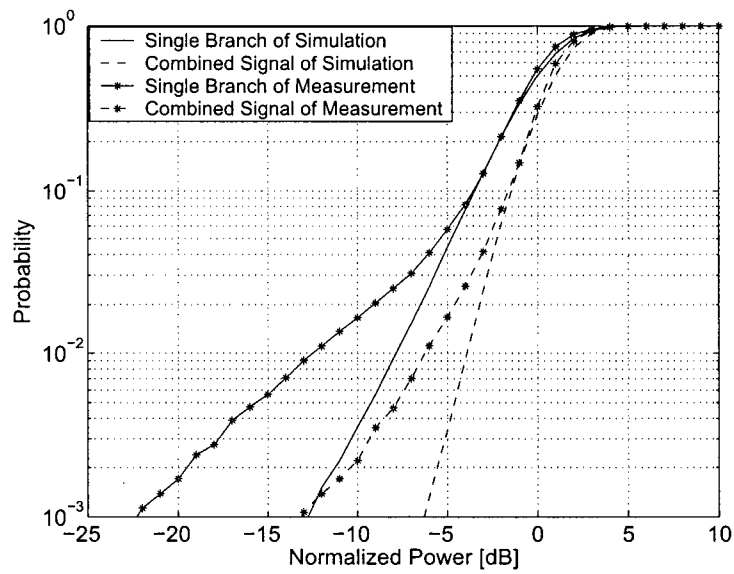
Figure 4.4: The CDF of single and selection combined envelopes for simulation and measurement
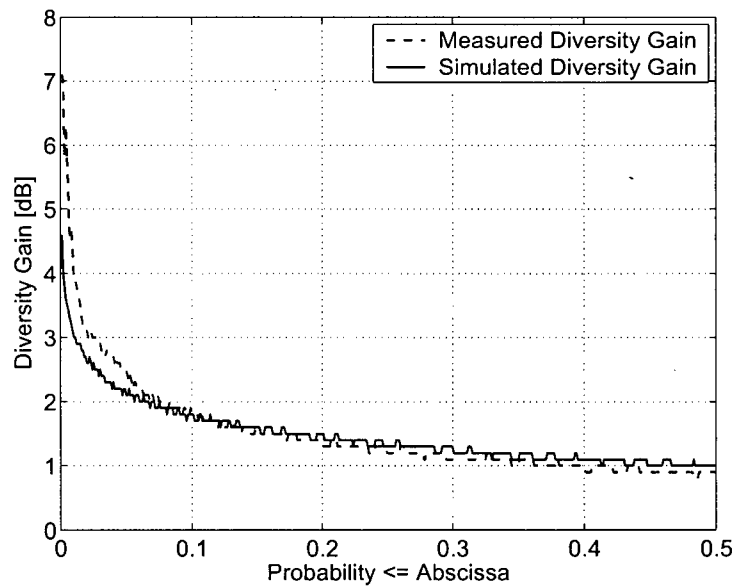
Figure 4.5: The diversity gain for simulated and measured signal envelopes

4.4 Simulation Results

As an illustrative example, the computer simulations were conducted by assuming the equal power and Rician K-factor on both branches. This avoided complications associated with the small variation in the local mean levels that are observed in practice.

Figure 4.6 shows the cumulative distribution for single and selection-combined fading envelopes as a function of antenna spacing. These envelopes are generated with Rician K-factor equal to 5 and use the average measurement results of envelope correlation for MacLeod 323, as shown in Figure 3.22. For clarity, the plot only shows the CDF curve for antenna separation $d = 0.25\lambda$, 0.5λ, 0.75λ and 1λ. We can see a significant improvement with respect to the single branch performance is observed for all the antenna separations from $d = 0.25\lambda$ to 1λ. We also note that the CDFs for antenna separation greater than 0.5λ are almost indistinguishable from each other, especially for large outage probability.

Figure 4.7 shows the estimation of diversity gain for different reliability levels, which are the probability levels that normalized received signal power exceeds a given threshold. Using selection diversity combining, diversity gains are 2.4 dB, 3.0 dB and 4.7 dB for 90%, 95% and 99% reliability at $d = 0.5\lambda$, while the diversity gains can reach as high as 2.5 dB, 3.2 dB and 5.2 dB at $d = \lambda$. From the plot, we can see that the diversity gains becomes saturated as the antenna spacing becomes larger than 0.5λ and the corresponding spatial correlations drop below 0.2.

Rician K-factor equal to 5 is typically considered to be a medium K-factor. In order to reveal the diversity performance in low and high Rician K-factor environments, we also performed simulations with K-factor equal to 0 and 10. When $K = 0$ the power in the fixed component is equal to zero and the Rician distributed envelope reduces to Rayleigh. This is an extreme scenario which is seldom observed for indoor fixed wireless channels. However, this scenario will help build our intuition concerning

the effectiveness of space diversity in similar low K-factor environments. The CDF for single and combined fading envelopes as $K = 10$ and $K = 0$ are plotted in Figure 4.8 and 4.10, as Figure 4.9 and 4.11 depict the diversity gains respectively. From the diversity gain plots, we can see that when $K = 10$, the maximum diversity gains can be achieved are 3.0 dB at 99% reliability, while, when $K = 0$, the diversity gains can reach 9.8 dB at the same level of reliability. The estimation results of diversity gain for MacLeod 323 and 458 are summarized in Table 4.1 and 4.2 respectively.

We compared the estimated diversity gains for $K = 0$, *i.e.*, Rayleigh distribution, with the results of traditional theoretical analysis [18], small variations (within 2%) were observed due to the limited sample size of simulation.

Table 4.1: Estimation of Diversity Gain for MacLeod 323 with 90, 95 and 99% Reliability Levels

Antenna Spacing	d/λ	0.125	0.25	0.375	0.5	0.625	0.75	0.875	1.0
Cross-correlation	ρ	0.64	0.55	0.36	0.24	0.18	0.19	0.08	0.13
Diversity Gain	90%	1.1	1.3	1.5	1.6	1.7	1.7	1.7	1.7
in dB	95%	1.4	1.5	1.8	2.0	2.0	2.0	2.1	2.0
with K=10	99%	2.1	2.2	2.6	2.6	3.0	2.8	3.0	3.0
Diversity Gain	90%	1.8	1.9	2.3	2.4	2.5	2.5	2.6	2.5
in dB	95%	2.2	2.5	2.9	3.0	3.2	3.2	3.3	3.2
with K=5	99%	3.8	4.2	4.7	4.7	5.2	5.2	5.2	5.2
Diversity Gain	90%	3.9	4.1	4.7	5.0	5.3	5.2	5.5	5.4
in dB	95%	5.1	5.2	6.0	6.4	6.6	6.5	6.7	6.7
with K=0	99%	8.2	8.2	9.3	9.7	9.8	9.8	9.8	9.8

Table 4.2: Estimation of Diversity Gain for MacLeod 458 with 90, 95 and 99% Reliability Levels

Antenna Spacing	d/λ	0.125	0.25	0.375	0.5	0.625	0.75	0.875	1.0
Cross-correlation	ρ	0.52	0.40	0.34	0.18	0.12	0.14	0.02	0.05
Diversity Gain	90%	1.3	1.4	1.5	1.7	1.8	1.7	1.9	1.8
in dB	95%	1.6	1.7	1.7	1.9	2.1	2.1	2.3	2.2
with K=10	99%	2.1	2.5	2.4	2.9	3.0	3.0	3.2	3.1
Diversity Gain	90%	1.9	2.1	2.1	2.4	2.5	2.5	2.7	2.7
in dB	95%	2.4	2.5	2.7	3.1	3.3	3.2	3.4	3.3
with K=5	99%	4.3	4.4	4.5	4.9	5.1	5.0	5.6	5.4
Diversity Gain	90%	4.4	4.7	4.9	5.2	5.2	5.2	5.5	5.4
in dB	95%	5.7	6.1	6.2	6.7	6.7	6.7	6.8	6.8
with K=0	99%	8.8	9.2	9.4	10.1	10.1	10.1	10.1	10.1
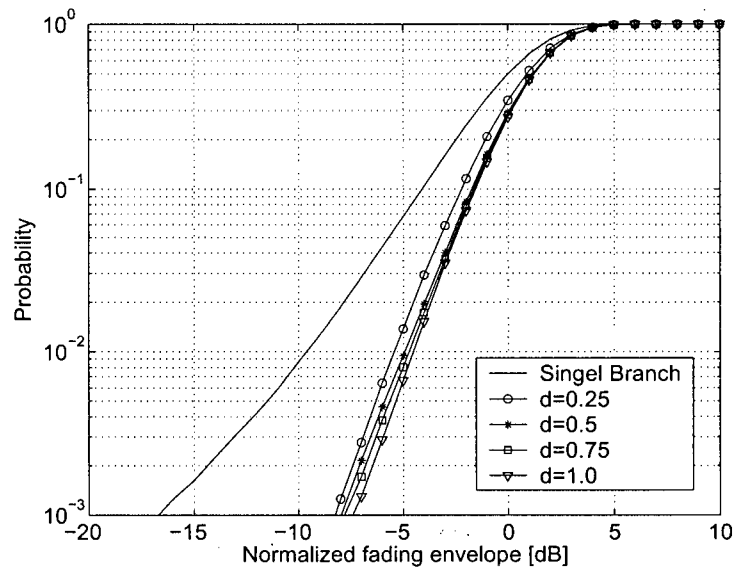
Figure 4.6: The CDFs for single and selection combined fading envelopes with K=5
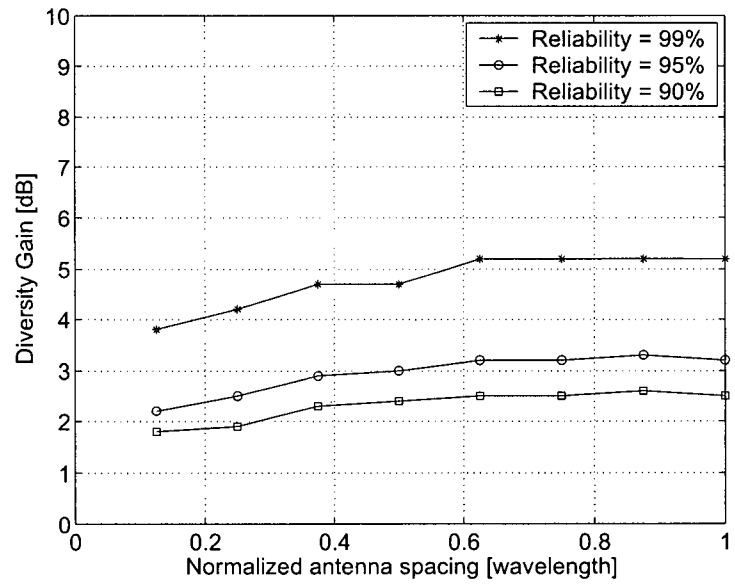
Figure 4.7: Diversity gain as a function of antenna spacing with different reliability levels when K=5
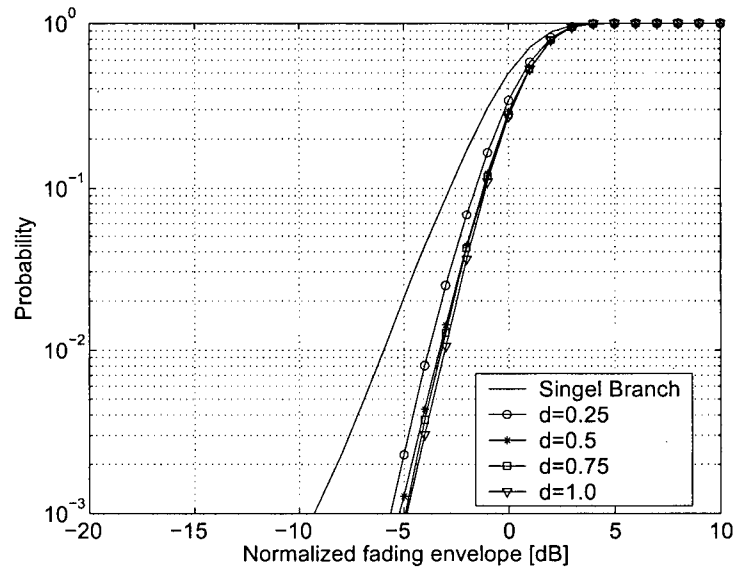
Figure 4.8: The CDFs for single and selection combined fading envelopes with K=10
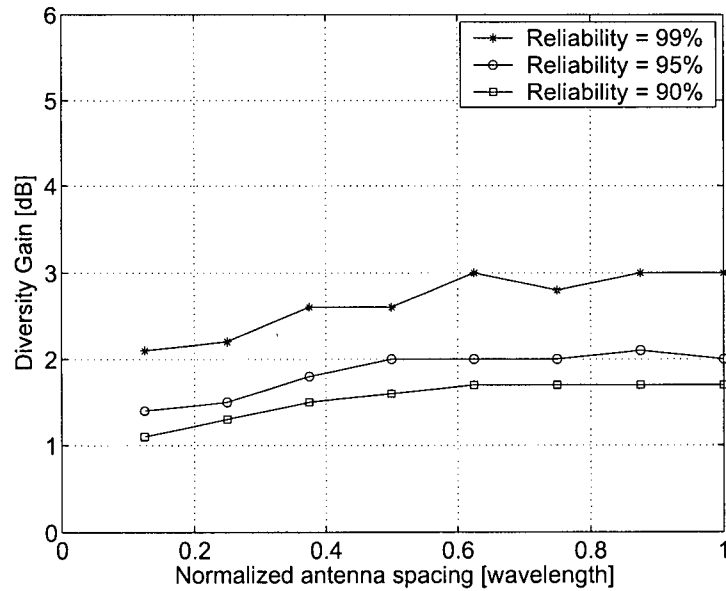
Figure 4.9: Diversity gain as a function of antenna spacing with different reliability levels when K=10
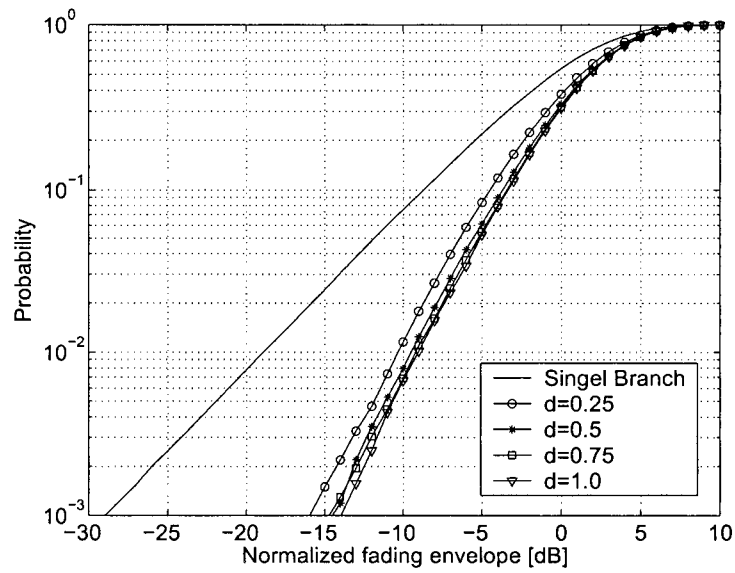
Figure 4.10: The CDFs for single and selection combined fading envelopes with K=0
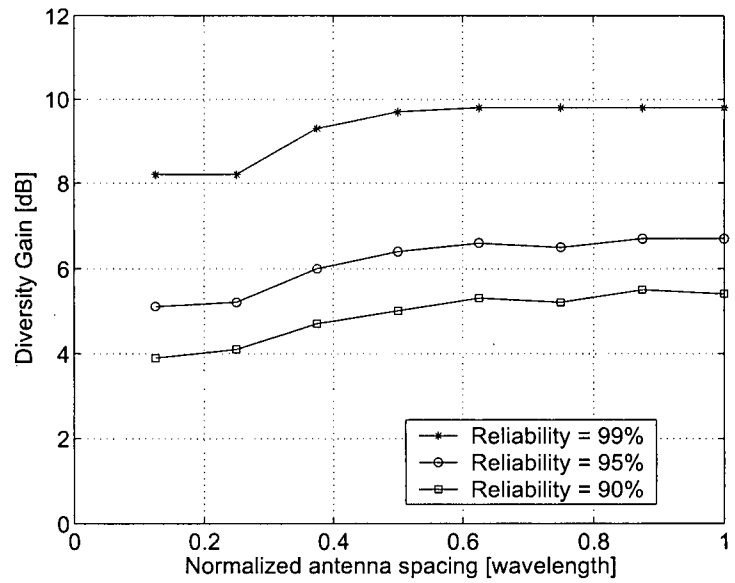
Figure 4.11: Diversity gain as a function of antenna spacing with different reliability levels when K=0

4.5 Summary

In this chapter, we showed how measurement-based models can form the basis for dynamic simulations of space diversity channels in indoor fixed wireless environments. These simulations incorporated the estimated spatial correlation and Doppler spectra presented in Chapter 3 to generate two correlated Rician fading envelopes with known K-factor, which can be treated as an indicator of environment change. We then estimated the diversity gain based on the simulated dual branch signals under the simplifying assumption that the mean signal strength on both branches are identical.

Considering a typical environment with Rician K-factor equal to 5, diversity gains at a 99% reliability level are as high as 4.9 and 5.4 dB for half- and one-wavelength antenna spacings, respectively. For a channel with a very strong specular component, *e.g.*, with $K = 10$, the corresponding diversity gains drop to 2.9 and 3.1 dB, while for a very severely scattered environment where Rayleigh fading envelopes are observed, the diversity gains will increase to around 10 dB for one-wavelength antenna spacings, which is consistent with the results of theoretical analysis..

Chapter 5

Conclusion and Recommendations

5.1 Conclusion

In this thesis, we have employed a measurement-based approach to investigate the effectiveness of space diversity in indoor fixed wireless environments where body shadowing (blockage of the line-of-sight between the transmitter and receiver by the movement of people) is a significant impairment. The results of our work are as follows:

In Chapter 2, we presented simulation results that give the sample duration required to accurately estimate path gain and Rician K-factor given the parameters of the Doppler spectrum (type and cut-off) and the sample rate. This is a useful result for those planning measurement campaigns in indoor fixed wireless environment.

In Chapter 3, we presented measurement results that show the received signal envelope follows the Rician distribution when people move between the transmitter and receiver. We also revealed details of the manner in which body shadowing affects the shape of the Doppler spectrum observed in indoor fixed wireless environments. In particular, we showed that body movement can give rise to significant sidebands in the Doppler spectrum. Finally, we compared theoretical predictions of spatial correlation as a function of antenna spacing to the measurement results and found reasonable agreement. The results give us confidence that our measurement system is suitable for use in more ambitious measurement campaigns in the future.

In Chapter 4, we showed how measurement-based models could be used in dynamic simulations of space diversity channels in indoor fixed wireless environments. Considering a typical environment with Rician K-factor equal to 5, diversity gains

at a 99% reliability level are as high as 4.9 and 5.4 dB for half- and one-wavelength antenna spacings, respectively. For a channel with a strong specular component, *e.g.*, with $K = 10$, the corresponding diversity gains drop to 2.9 and 3.1 dB, while for a very severely scattered environment where Rayleigh fading envelopes are observed, the diversity gains will increase to around 10 dB for one-wavelength antenna spacings, which is consistent with the results of theoretical analysis.

5.2 Recommendations for Future Work

- *Three-way diversity in indoor and microcell environments.* Indoor and microcell environments are a diverse collection. The angle-of-arrival distribution in such environments may vary from highly directive to highly diffuse. It is well known that two-way space diversity performance degrades as the AoA approaches the axis of the array although the degradation will be less dependent on AoA as the angle spread increases. We anticipate that angle spread will broaden as we move from open to closed areas. We recommend that a study be conducted in order to determine the extent to which novel diversity schemes, including various types of three-way diversity, provide improvement.

- *Doppler spectra in body shadowing environments.* The sideband structures observed in the Doppler spectra presented in Chapter 3 are not well accounted for in the literature. We recommend that steps be taken to modify the simulation methodology employed in [22] with the propagation model used in [31] to account for this effect.

- *Effect of Doppler spectrum on the number of required samples.* We recommend that steps be taken to determine how the number of samples required to estimate Rician K is affected by the shape of the Doppler spectrum, *e.g.*, classical U-shape, central peaky shape and the new type of Doppler spectrum observed in

Chapter 3.

Bibliography

[1] T. S. Rappaport, *Wireless Communications: Principles and Practice.* New Jersey: Prentice-Hall, 1996.

[2] J. H. Tarng, R. S. Chang, J. M. Huang, and Y. M. Tu, "A new and efficient hybrid model for estimating space diversity in indoor environment," *IEEE Trans. Veh. Technol.*, vol. 49, no. 2, pp. 457–466, Mar. 2000.

[3] J. A. Tsai, R. M. Buehrer, and B. D. Woerner, "The impact of AOA energy distribution on the spatial fading correlation of linear antenna array," in *Proc. IEEE VTC02 (Spring)*, vol. 2, May 2002, pp. 933–937.

[4] R. H. Clarke, "A statistical theory of mobile-radio reception," *Bell Syst. Tech. J.*, pp. 957–1000, July-Aug 1968.

[5] R. G. Vaughan and N. L. Scott, "Closely spaced monopoles for mobile communications," *Radio Sci.*, vol. 28, no. 6, pp. 1259–1266, Nov. 1993.

[6] W. C. Y. Lee, *Mobile Communications Engineering.* New York: McGraw Hill Publications, 1985.

[7] J. Lemieux, M. S. El-Tanany, and H. M. Hafez, "Experimental evaluation of space/frequency/polarization diversity in the indoor wireless channel," *IEEE Trans. Veh. Technol.*, vol. 40, pp. 569–573, Aug. 1991.

[8] S. R. Todd, M. S. El-Tanany, and S. A. Mahmoud, "Space and frequency diversity measurements of the 1.7 GHz indoor radio channel using a four-branch receiver," *IEEE Trans. Veh. Technol.*, vol. 41, pp. 312–320, Aug. 1992.

[9] G. E. Corazza, V. Degli-Esposti, M. Frullone, and G. Riva, "A characterization of indoor space and frequency diversity by ray-tracing modeling," *IEEE J. Select. Areas Commun.*, vol. 14, no. 3, pp. 411–419, 1996.

[10] K. A. Remley, H. R. Anderson, and A. Weisshar, "Improving the accuracy of ray-tracing techniques for indoor propagation modeling," *IEEE Trans. Veh. Technol.*, vol. 49, pp. 2350–2357, Nov. 2000.

[11] D. Parsons, *The Mobile Radio Propagation Channel.* New York: Halsted, 1992.

[12] G. L. Stuber, *Principles of Mobile Communication.* Norwell, MA: Kluwer Academic Publishers, 2001.

[13] C. Tepedelenlioglu, A. Abdi, and G. B. Giannakis, "The Ricean K-factor: estimation and performance analysis," *IEEE Trans. Wireless Commun.*, vol. 2, no. 4, pp. 799–810, July 2003.

[14] K. K. Talukdar and W. D. Lawing, "Estimation of the parameters of the Rice distribution," *J. Acoust. Soc. Amer.*, vol. 89, pp. 1193–1197, 1991.

[15] L. J. Greenstein, D. G. Michelson, and V. Erceg, "Moment-method estimation of the Ricean K-factor," *IEEE Commun. Lett.*, vol. 3, pp. 175–176, June 1999.

[16] A. Abdi, C. Tepedelenlioglu, G. B. Giannakis, and M. Kaveh, "On the estimation of the K parameter for the Rice fading distribution," *IEEE Commun. Lett.*, vol. 5, pp. 92–94, Mar. 2001.

[17] H. Cramer, *Mathematical Methods of Statistics.* Princeton, NJ: Princeton Univ. Press., 1946.

[18] W. C. Jakes, *Microwave Mobile Communications.* New York: Wiley, 1974.

[19] A. Domazetovic, L. J. Greenstein, N. B. Mandayam, and I. Seskar, "Estimating the Doppler spectrum of a short-range fixed wireless channel," *IEEE Commun. Lett.*, vol. 7, no. 5, pp. 227–229, May 2003.

[20] D. S. Baum, D. Gore, R. Nabar, S. Panchanathan, K. V. S. Hari, V. Erceg, and A. J. Paulraj, "Measurement and characterization of broadband MIMO fixed wireless channels at 2.5 GHz," in *Proc. IEEE IPWC'00*, Dec. 2000, pp. 203–206.

[21] S. J. Howard and K. Pahlavan, "Doppler spread measurements of indoor radio channel," *Electron. Lett.*, vol. 26, no. 2, pp. 107–109, Jan. 1990.

[22] S. Thoen, L. V. D. Perre, and M. Engels, "Modeling the channel time-variance for fixed wireless communications," *IEEE Commun. Lett.*, vol. 6, pp. 331–333, Aug. 2002.

[23] D. J. Young and N. C. Beaulieu, "A quantitative evaluation of generation methods for correlated Rayleigh random variates," in *Proc. IEEE GLOBECOM'98.*, Nov. 1998, pp. 3332 – 3337.

[24] ——, "The generation of correlated Rayleigh random variate by inverse discrete Fourier transform," *IEEE Trans. Commun.*, vol. 48, no. 7, pp. 1114–1127, July 2000.

[25] D. Verdin and T. Tozer, "Generating a fading process for the simulation of land-mobile radio communications," *Electronics Letters*, vol. 29, no. 23, pp. 2011–2012, Nov. 1993.

[26] R. J. C. Bultitude, "Measurement characterization and modeling of indoor 800/900 MHz radio channels for digital communications," *IEEE Commun. Mag.*, vol. 5, no. 6, pp. 5–12, Feb. 1987.

[27] ——, "A comparison of indoor radio propagation characteristics at 910 MHz and 1.75 GHz," *IEEE J. Select. Areas Commun.*, vol. 7, no. 1, pp. 20–30, Jan. 1989.

[28] T. S. Rappaport and C. D. McGillem, "UHF fading in factories," *IEEE J. Select. Areas Commun.*, vol. 7, pp. 40–48, 1989.

[29] H. Hashemi, M. McGuire, T. Vlasschaert, and D. Tholl, "Measurements and modeling of temporal variations of the indoor radio propagation channel," *IEEE Trans. Veh. Technol.*, vol. 43, pp. 733–737, Aug. 1994.

[30] J. S. Colburn, Y. Rahmat-Samii, M. A. Jensen, and G. J. Pottie, "Evaluation of personal communications dual-antenna handset diversity performance," *IEEE Trans. Veh. Technol.*, vol. 47, p. 737746, Aug. 1998.

[31] R. M. Narayanan and M. Dawood, "Doppler estimation using a coherent ultrawide-band random noise radar," *IEEE Trans. Antennas Propagat.*, vol. 48, no. 6, pp. 868–878, June 2000.

[32] B. M. Green and M. A. Jensen, "Diversity performance of dual-antenna handsets near operator tissue," *IEEE Trans. Antennas Propagat.*, vol. 48, no. 7, pp. 1017–1024, July 2000.

[33] B. Natarajan, C. Nassar, and V. Chandrasekhar, "Generation of correlated Rayleigh fading envelopes for spread spectrum applications," *IEEE Commun. Lett*, vol. 4, pp. 9–11, Jan. 2000.